Stratospheric aerosol characteristics from SCIAMACHY limb observations: 2-parameter retrieval

Christine Pohl[1], Felix Wrana[2], Alexei Rozanov[1], Terry Deshler[3], Elizaveta Malinina[4], Christian von Savigny[2], Landon A. Rieger[5], Adam E. Bourassa[5], and John P. Burrows[1]

[1]Institute of Environmental Physics, University of Bremen, Bremen, Germany
[2]Institute of Physics, University of Greifswald, Greifswald, Germany
[3]Department of Atmospheric Science, University of Wyoming, Laramie, Wyoming, USA
[4]Canadian Centre for Climate Modeling and Analysis, Environment and Climate Change Canada, Victoria, British Columbia, Canada
[5]Institute of Space and Atmospheric Studies, University of Saskatchewan, Saskatoon, Canada

Correspondence: Christine Pohl (cpohl@iup.physik.uni-bremen.de)

Abstract.

Stratospheric aerosols play a key role in atmospheric chemistry and climate. Their particle size is a crucial factor controlling the microphysical, radiative, and chemical aerosol processes in the stratosphere. Despite its importance, available observations on aerosol particle size are rather sparse. This limits our understanding and knowledge about the mechanisms and importance of chemical and climate aerosol feedbacks. The retrieval described by Malinina et al. (2018) provides the stratospheric particle size distribution (PSD) from SCIAMACHY limb observations in the tropics. This algorithm has now been improved and extended to work on the entire globe. Two PSD parameters of a unimodal lognormal PSD, the median radius and the geometric standard deviation, are retrieved between 18 and 35 km altitude from SCIAMACHY limb observations by a multi-wavelength non-linear regularized inversion. This assumes a fixed number density profile. The extinction coefficient and the effective radius are calculated. The effective Lambertian surface albedo pre-retrieved from coinciding SCIAMACHY nadir observations is integrated into the retrieval algorithm to mitigate the influence of the surface albedo on the retrieval results. The aerosol characteristics from SCIAMACHY are compared with in-situ balloon-borne measurements from Laramie, Wyoming, and retrievals from the satellite instruments SAGE II, SAGE III, and OSIRIS. In the northern hemisphere, the median radius differs by less than 27 % and the geometric standard deviation by less than 11 % from both balloon-borne and SAGE III data. Differences are mainly attributed to errors in the assumed a priori number density profile. Globally, the SCIAMACHY extinction coefficients at 750 nm deviate by less than 35 % from SAGE II, SAGE III, and OSIRIS data. The effective radius from SCIAMACHY, balloon-borne measurements, and SAGE III agree within about 18 % while the effective radius based on SAGE II measurements is systematically larger. The novel data set containing the effective radius and the aerosol extinction coefficient at 525, 750, and 1020 nm from SCIAMACHY observations is publicly available.

1 Introduction

Stratospheric aerosols are well known to play a key role in atmospheric chemistry and climate (Kremser et al., 2016). They form a distinct layer, the so-called "Junge layer", in the altitude range between 15 and 35 km. The maximum concentration is typically around 20 km. This aerosol layer consists mainly of hydrated sulfuric acid supplemented by small amounts of meteorite and other non-sulfate particles (Kremser et al., 2016).

The background aerosol loading in the stratosphere is in a quasi-stationary equilibrium due to continuous natural and anthropogenic emissions of OCS and SO_2 as well as evaporation and sedimentation processes, with seasonal and quasi-biennial oscillations (Deshler et al., 2006). Occasionally, the background state is overlaid by aerosols originating from transient but sulfur-rich volcanic eruptions (McCormick et al., 1995; Andersson et al., 2015; Friberg et al., 2018; Kloss et al., 2021) and biomass burning events (Siddaway and Petelina, 2011; Bourassa et al., 2019; Ohneiser et al., 2020; Das et al., 2021). The aerosols entrained in the stratosphere are dispersed on a global scale by advection and self-generated thermal convection. Microphysical processes such as nucleation, coagulation, and condensation control the spatiotemporal variation of the total aerosol number concentration and size distribution. Aerosols remain in the stratosphere for several months to years until evaporation at the top of the aerosol layer (above 32-35 km altitude) and sedimentation processes return the stratospheric aerosol level to background conditions (Kremser et al., 2016).

Volcanic and wildfire perturbations significantly increase the stratospheric aerosol optical depth (SAOD) on a global scale, which have a short-term impact on the Earth's radiative budget (Malinina et al., 2021; Sellitto et al., 2022). The enhanced stratospheric short-wave scattering and long-wave absorption typically force a cooling of the surface and a heating of the stratosphere. This triggers a series of responses in the internal dynamics responsible for the climate system, which are summarized in Marshall et al. (2022). Among others, investigations have noted changes in the North Atlantic Circulation (Hermanson et al., 2020), El Niño-Southern Oscillation (Khodri et al., 2017), Atlantic Meridional Overturning Circulation (Pausata et al., 2015), atmospheric dynamics (Toohey et al., 2014), and quasi-biennial oscillation (DallaSanta et al., 2021). Furthermore, there is evidence of weaker monsoons (Liu et al., 2016), reduced precipitation (Iles et al., 2013), and a shifted Inter-Tropical Convergence Zone (Colose et al., 2016).

Even small amounts of aerosols play a significant role as catalysers in stratospheric chemistry. Heterogeneous chemical reactions on the aerosol droplet surface increase the amount of reactive chlorine and hydrogen oxide radicals as well as reduce the amount of nitrogen oxide (NO, NO_2) in the surrounding atmosphere (Fahey et al., 1993; Solomon et al., 1996). These reactions lead to an imbalance in the photochemical cycle of ozone loss and production and thus to ozone depletion. Furthermore, stratospheric aerosols serve as condensation nuclei for polar stratospheric cloud formation (Ebert et al., 2016).

The climatic and chemical significance of stratospheric aerosols makes an accurate knowledge of the microphysical and radiative aerosol properties important for the assessment of aerosol feedback mechanisms. This knowledge is obtained from in-situ (balloon and aircraft), ground-based, and satellite measurements, which are summarized and discussed in, e. g., Thomason and Peter (2006) and Kremser et al. (2016).

The observations of stratospheric aerosols are used for several purposes. Analysing measurements allows conclusions to be drawn about the evolution and interaction of stratospheric aerosols. Information obtained from aerosol observations contributes to the development of aerosol microphysical modules (Vignati et al., 2004), aerosol transport schemes (Grieser and Schönwiese, 1999), and volcanic forcing emulators (Toohey et al., 2016; Aubry et al., 2020). The observed aerosol characteristics are summarized in aerosol climatologies (e. g., Mills et al., 2016; Thomason et al., 2018; Kovilakam et al., 2020), which are used to create volcanic aerosol forcing sets (Stenchikov et al., 1998; Arfeuille et al., 2013; Sato et al., 2016). Those can be subsequently utilized in climate impact studies (Toohey et al., 2014; Brühl et al., 2015). Furthermore, aerosol observations are required to test the reliability of climate models. Recent studies show discrepancies between observations and simulations (e. g., Chylek et al., 2020; Tejedor et al., 2021), indicating that knowledge about stratospheric aerosols is still incomplete. Accordingly, aerosol observations are used to adjust or constrain aerosol plumes in climate models (Das et al., 2021; Schallock et al., 2023) to enable more realistic simulations and more accurate estimates of aerosol radiative forcing. In addition, observations of post-volcanic aerosol distributions provide new insights into effectiveness and impacts of potential geoengineering concepts (Robock et al., 2013).

The aerosol particle size is one of the main parameters in model simulations as it controls the microphysical, radiative, and chemical aerosol processes (Kremser et al., 2016). The knowledge of particle size is therefore a key factor in describing stratospheric aerosol evolution and associated climate response. Despite its importance, available observations on aerosol particle size are rather limited. Valuable in-situ (Deshler et al., 2019), airborne (McLinden et al., 1999), and ground-based measurements (Ugolnikov and Maslov, 2018; Zalach et al., 2019) of aerosol sizes are rare and localised. Retrievals of the size distribution from the Stratospheric Aerosol and Gas Experiment (SAGE) series data (Bingen et al., 2004; Wurl et al., 2010; Damadeo et al., 2013; Wrana et al., 2021) are global albeit the occultation measurements suffer from a rather coarse spatial sampling and limited coverage. Aerosol particle size data sets with dense spatial sampling were firstly obtained from the Optical Spectrograph and InfraRed Imager System (OSIRIS) (Bourassa et al., 2008; Rieger et al., 2014) and the Scanning Imaging Absorption Spectrometer for Atmospheric Cartography (SCIAMACHY) limb observations (Malinina et al., 2018). The latter data set is restricted to the tropics, while the former data set is no longer updated.

In this study, the algorithm from Malinina et al. (2018) developed to derive the stratospheric aerosol particle size distribution (PSD) in the tropics is extended to work on the entire globe, here. Similar to Malinina et al. (2018), the median radius and the geometric standard deviation of a unimodal lognormal distribution are retrieved from SCIAMACHY limb scatter observations by assuming a fixed number density. From that, the effective radius and the extinction coefficient are calculated. The retrieval uses the effective Lambertian surface albedo pre-retrieved from coinciding SCIAMACHY nadir measurements. This mitigates the influence of surface reflection on the retrieval results. The resulting data set contains the PSD parameters in the northern hemisphere, as well as the effective radius and the extinction coefficient at 525, 750, and 1020 nm for the entire globe. The SCIAMACHY limb radiance in the southern hemisphere is less sensitive to PSD parameters making it difficult to retrieve them separately (Sect. 6).

The manuscript is structured as follows: After an introduction to the relevant aerosol characteristics in Sect. 2, the SCIA-MACHY instrument and the retrieval algorithm is described in Sects. 3 and 4. Comparison data sets and satellite instruments

are presented in Sect. 5. In Sect. 6, the retrieval performance is investigated using a synthetically generated data set. The SCIAMACHY-retrieved and calculated aerosol characteristics are compared with balloon-borne measurements and satellite data products in Sect. 7. The comparison results are discussed in Sect. 8, followed by a conclusion in Sect. 9.

2 Stratospheric aerosol characteristics

The PSD of stratospheric aerosols is represented by a lognormal distribution, which has a different number of modes depending on the application (Deshler et al., 2003; Brühl et al., 2012; von Savigny and Hoffmann, 2020). Retrievals from space-borne measurements usually adopt a unimodal lognormal PSD (e.g., Bingen et al., 2004; Rieger et al., 2014; Malinina et al., 2018; Wrana et al., 2021):

$$n(r) = \frac{N}{\sqrt{2\pi}\ln\sigma_{\mathrm{g}}\,r}\exp\left(-\frac{(\ln r - \ln r_g)^2}{2\ln^2\sigma_{\mathrm{g}}}\right), \tag{1}$$

where the number density n of particles with radius r is defined by the total number density N, the geometric mean or median radius r_g, and the geometric standard deviation σ_g (see Appendix A for derivation of the equation and explanation of the nomenclature). The assumption of a unimodal PSD is advantageous because it describes the prevailing PSD relatively well with only three degrees of freedom.

Another prevalent parameter to describe the aerosol particle size is the effective radius. It is defined by the ratio of the third to the second moment of the PSD, i. e., the ratio of the total particle volume V to the total particle surface area A per unit volume times 3:

$$r_{\mathrm{eff}} = \frac{3V}{A} = \frac{\int r\,\pi\,r^2\,n(r)\,\mathrm{d}r}{\int \pi\,r^2\,n(r)\,\mathrm{d}r}. \tag{2}$$

The right hand side of Eq. (2) indicates that r_{eff} is a weighted average with the cross sectional area as the weighting factor. Although, r_{eff} does not represent any PSD characteristics, it is useful in scattering optics. As the particle size determines the scattering probability, r_{eff} indicates a typical aerosol particle size in the prevailing scattered radiation field. Different PSDs can have identical effective radii and scattering properties. The effective radius thus unifies the results from stratospheric aerosol particle size retrievals independent of their PSD-based assumptions and facilitates their comparison (Mishchenko and Travis, 1997).

For a unimodal lognormal PSD, r_{eff} is related to r_{g} and σ_{g} by:

$$r_{\mathrm{eff}} = r_{\mathrm{g}}\exp(2.5\ln^2\sigma_{\mathrm{g}}). \tag{3}$$

The optical properties of aerosols can be characterized by, e. g., their extinction coefficient. It is defined as:

$$Ext(\lambda) = \int \beta_{\mathrm{aer}}(r, \lambda, \mathfrak{m})\,n(r)\,\mathrm{d}r, \tag{4}$$

where β_{aer} is the aerosol extinction cross section calculated by Mie theory and $\mathfrak{m}$ is the aerosol refractive index at wavelength λ. The ratio of aerosol extinction coefficients at two different wavelengths provides the Ångstrom exponent α (Ångström,

1929):

$$\frac{Ext(\lambda_1)}{Ext(\lambda_2)} = \left(\frac{\lambda_1}{\lambda_2}\right)^{\alpha}. \tag{5}$$

The Ångstrom exponent α is only an approximate measure of the aerosol particle size because it depends on the choice of
120   wavelength pair. Furthermore, an infinite number of PSD parameter combinations can result in the same α (Malinina et al., 2019). Thus, the Ångstrom exponent in Eq. (5) is only used to calculate the extinction coefficients for desired wavelengths. Note that these kind of calculations may be subject to uncertainties for the reasons mentioned above.

3   SCIAMACHY observations

The Scanning Imaging Absorption Spectrometer for Atmospheric Cartography (SCIAMACHY) was operated aboard the Eu-
125   ropean Environmental Satellite (Envisat). It was launched on 1 March 2002 into a sun-synchronous orbit at an altitude of about 800 km with a local descending node equator crossing time of 10 am. SCIAMACHY's measurements started in August 2002 and ended in April 2012 after communications with Envisat were lost.

SCIAMACHY measured the scattered solar radiance in limb and nadir geometry, the attenuated solar and lunar radiance in occultation geometry as well as the extraterrestrial solar irradiance and lunar radiance. The radiance in the limb and nadir ge-
130   ometry as well as the solar irradiance are used for the PSD retrieval. Limb and nadir measurements were performed alternately on the day side of the orbit, the solar irradiance once per orbit. The radiation was detected by a grating spectrometer in eight wavelength bands covering the spectral range between 214 and 2386 nm. The spectral resolution depends on the wavelength and is between 0.2 and 1.5 nm.

In the nadir scan mode, the instrument observed the Earth's scenery below the satellite using a whisk-broom scanning system.
135   Each orbital scan has a swath width of 960 km, i. e., a field of view of ± 32 °. Typically, it consists of four scan targets (pixels) per whisk-broom line at viewing zenith angles (VZAs) of about ± 9° and ± 26 °. The footprint size of each pixel depends on the scan speed, measurement integration time, and observation geometry and is usually 30 km along-track and 240 km (60 km – best case) across-track. After 13 whisk-broom lines were recorded, SCIAMACHY switched to the limb viewing geometry.

In the limb scan mode, the instrument observed the scattered solar radiance tangential to the Earth's surface at tangent heights
140   between -3 and about 100 km in steps of 3.3 km. The radiation was typically sampled at four different viewing azimuth angles at a constant elevation angle before the optics tilted to the next scanning elevation. The viewing azimuth angles were carefully chosen in order to match the geographic location of the limb scatter measurement with the individual scenes of subsequent nadir measurements. In total, four measurement profiles of spectral radiances were recorded with a vertical resolution of 2.6 km and a horizontal resolution of about 400 km along-track and 240 km across-track. This results in a total swath width of 960 km.
145   One limb observation sequence usually lasted 60 s.

According to the scanning geometry and sampling, SCIAMACHY achieved global coverage at the equator after 6 days. Further information about the instrument is provided in, e. g., Burrows et al. (1995), Bovensmann et al. (1999), and Gottwald and Bovensmann (2010).

4 SCIAMACHY version 2.0 aerosol retrieval

150 Malinina et al. (2018) retrieved the stratospheric PSD and the effective Lambertian surface albedo simultaneously to account for the influence of the surface reflectance on the measured limb radiance. However, the algorithm cannot reliably distinguish whether, e. g., an increase in the measurement signal is caused by a higher surface albedo or by a stronger scattering of stratospheric aerosols. Therefore, we split the aerosol retrieval algorithm in two steps: First, the effective Lambertian surface albedo is retrieved from coinciding SCIAMACHY nadir radiances. Then, the albedo is used as a first guess to retrieve vertical

155 profiles of r_g and σ_g from SCIAMACHY limb radiances.

Both retrieval steps are based on the linearization of the forward model $\mathbf{F}(\mathbf{x})$ around an initial guess state $\mathbf{x_0}$ (Rodgers, 2000):

$$\mathbf{y} - \mathbf{y_0} = \mathbf{K}(\mathbf{x} - \mathbf{x_0}) + \boldsymbol{\epsilon}, \tag{6}$$

where $\mathbf{y}$ and $\mathbf{y_0}$ are the measurement and initial guess vector, $\mathbf{K}$ is the weighting function or Jacobian matrix, $\mathbf{x}$ is the state

160 vector, and $\boldsymbol{\epsilon}$ is the noise vector containing the modelling, measurement, and linearization errors.

The measurement vector $\mathbf{y}$ contains the logarithms of sun-normalized SCIAMACHY radiances, averaged in the six wavelength ranges $748 - 752$, $805 - 809$, $868 - 872$, $1088 - 1092$, $1225 - 1245$, and $1294 - 1306$ nm. Other wavelength bands are not taken into account because radiation at shorter wavelengths or between the selected wavelength bands is too strongly influenced by Rayleigh scattering and molecular absorption and radiation at longer wavelengths has too low signal-to-noise

165 ratios. According to the retrieval procedure, SCIAMACHY radiances from the nadir geometry are used in the first step, SCIA-MACHY radiances from the limb geometry are used in the second step. Here, only measured limb radiances between 18 and 35 km altitude are considered. The radiation from lower altitudes is too strongly influenced by scattering from molecules, clouds, and tropospheric aerosol contaminations while radiation above 35 km is influenced by stray-light.

The initial guess vector $\mathbf{y_0}$ contains the corresponding logarithms of sun-normalized radiances simulated by the radiative

170 transfer model SCIATRAN 4.1 (Rozanov et al., 2014; Mei et al., 2023) for the initial state vector $\mathbf{x_0}$.

The state vectors $\mathbf{x_0}$ and $\mathbf{x}$ contain the a priori quantities and the quantities to be retrieved, respectively. In the first step, these are the effective Lambertian surface albedo values at the six wavelength bands mentioned above. In the second step, the state vectors contain the vertical profiles of r_g and σ_g between 18 and 35 km altitude as well as the effective Lambertian surface albedo at the six wavelength bands. The albedo values are auxiliary retrieval quantities. They are used to minimize influences

175 associated with the incorrect assumption of a Lambertian surface and thus improve the aerosol retrieval.

The weighting function matrix or Jacobian matrix $\mathbf{K}$ contains the partial derivatives of the forward model operator with respect to each state vector element (retrieval quantity).

A solution with respect to the state vector $\mathbf{x}$ in Eq. (6) is obtained by iterative minimization of the following weighted norm:

180 $$\|\mathbf{y} - \mathbf{y_0}\|^2_{\mathbf{S_y^{-1}}} + \|\mathbf{x} - \mathbf{x_0}\|^2_{\mathbf{S_a^{-1}}}, \tag{7}$$

where the noise covariance matrix $\mathbf{S_y}$ and the a priori covariance matrix $\mathbf{S_a}$ are the weight matrices. Their contents are explained in detail below. In this optimization method, we do not follow the maximum a posteriori method of Rodgers (2000), which assumes a fixed a priori state vector $\mathbf{x_0}$. Instead, we invert Eq. (6) analogous to Malinina et al. (2018) by the weighted regularized approach based on the zeroth-order Tikhonov method:

$$185 \quad \mathbf{x_{n+1}} = \mathbf{x_n} + \left(\mathbf{K_n^\top S_y^{-1} K_n} + \mathbf{S_a^{-1}} \right)^{-1} \mathbf{K_n^\top S_y^{-1}} \left(\mathbf{y} - \mathbf{y_n} \right), \qquad (8)$$

where $\mathbf{K_n} = \mathbf{K(x_n)}$ and $\mathbf{y_n} = \mathbf{F(x_n)}$. In this approach, the initial guess state $\mathbf{x_0}$ in iteration $n + 1$ is replaced by the state vector $\mathbf{x}$ obtained at the previous iteration n. This enables the final result to move far away from a priori values while strongly constraining each particular iterative step. The latter is necessary because of a strong non-linearity of the inverse problem and a correlation between the retrieval parameters.

Two convergence criteria are selected to terminate the iterative algorithm: Either the root mean square deviation between all simulated and measured radiances considered within the retrieval changes by less than 0.1 % or each state vector element (retrieval quantities) changes by less than 1 % in two consecutive iterations. If both criteria are not fulfilled, the algorithm is aborted after 30 iterations.

Finally, the retrieved PSD parameters and the assumed number density are used to calculate the effective radius (Eq. (3)) and the extinction coefficient (Eq. (4)) of the aerosol particles. We calculate the aerosol extinction coefficient at 750 nm to make it comparable with our previous SCIAMACHY v1.4 Ext product (Rieger et al., 2018). For the public, we also calculate the aerosol extinction coefficient at 525 and 1020 nm to enable a comparison with other satellite aerosol products. This general retrieval structure includes the following specific details.

In the albedo retrieval (first step), the measurement vector $\mathbf{y}$ contains the logarithms of normalized nadir radiances averaged along the track over all pixels of the corresponding nadir scan at constant VZA. Since each nadir scan contains 13 whisk-broom lines of four pixels each, four averaged radiance spectra at VZAs of about $\pm 9°$ and $\pm 26°$ are obtained from which the effective Lambertian albedo is retrieved. A constant albedo of 0.5 is assumed as a first guess. The a priori covariance matrix and the noise covariance matrix are chosen to be diagonal, i.e., no correlation between the radiances or the albedo of different wavelengths is assumed. The diagonal elements are set to $1e{-}2$ for the a priori covariance and to the signal-to-noise ratio of 1000 for the noise covariance matrix.

In the PSD retrieval (second step), the effective Lambertian surface albedo retrieved in the first step is used as the a priori information. The geographical locations of limb scatter and averaged nadir measurements may only differ by a maximum of 223 km, which corresponds to a latitudinal width of about $2°$. Otherwise, no PSD retrieval is performed.

The stratospheric aerosols are assumed to be located at altitudes between 12 and 46 km within an atmosphere of 0 % relative humidity. They are specified as a mixture of 75 % sulphuric acid and 25 % water. Their refractive indices are based on the OPAC database (Hess et al., 1998). The scattering phase functions as well as extinction and scattering coefficients are calculated employing Mie theory. Constant vertical profiles of the mode radius $R_{\mathrm{mod}} = 0.11\,\mu\mathrm{m}$ and $\sigma_{\mathrm{g}} = 1.37$ are assumed as a first guess. The values are chosen arbitrarily, but are realistic for background aerosol loadings (Deshler, 2008). If not stated

otherwise, the number density profile is based on the ECSTRA model climatology for aerosol background conditions (Fussen
215   and Bingen, 1999). It decreases exponentially from $22.83\,\mathrm{cm}^{-3}$ at 12 km to $0.03\,\mathrm{cm}^{-3}$ at 46 km altitude.

While r_g and σ_g are derived, N remains fixed for two reasons. First, by fixing one PSD parameter, the other two parameters
have a larger response to differences between simulated and measured limb radiances. Second, among the three PSD parame-
ters, a change of N has the least effect on the resulting limb radiance (Malinina et al., 2018). As a result, uncertainties caused
by a fixed N profile have less influence on the PSD retrieval than if r_g or σ_g are kept constant.

220   Profiles of r_g and σ_g are retrieved between 18 and 35 km altitude. Above 35 km, the PSD profile remains unchanged. Below
18 km, the PSD profile is scaled with the same factor as the lowermost retrieval tangent height. Within the iterative process,
R_mod and the surface albedo cannot become smaller than $0.05\,\mathrm{\mu m}$ and 0.015, respectively. The radius limit is lower than the
sensitivity limit of SCIAMACHY (Malinina et al., 2019). Surface albedo values below 0.015 usually do not occur. Both limits
are chosen to avoid unphysical results. No limits are set for σ_g.

225   Since three species are retrieved in the second step (r_g, σ_g, and the albedo), the a priori covariance matrix has to be set for
each species individually. In case of r_g and σ_g, the covariance matrix elements are calculated by:

$$[\mathbf{S_a}]_{j,k} = \varsigma^2 \exp\left(-\frac{|z_\mathrm{j} - z_\mathrm{k}|}{r_\mathrm{c}}\right), \tag{9}$$

where r_c is the correlation radius that is set to 3.3 km and z_j and z_k are the altitudes corresponding to the element (j,k). The
variances are set to $\varsigma^2 = 2.5\mathrm{e}{-7}\,\mathrm{\mu m}^2$ in case of r_g and to $\varsigma^2 = 2.5\mathrm{e}{-7}$ in case of σ_g. The values are selected as a trade-off
230   between the numerical stability and a priori sensitivity. Note that instead of relative variances (Malinina et al., 2018), we use
absolute values to retain a constant variance within the iterative process.

The a priori covariance matrix of the albedo is a diagonal matrix. Each diagonal entry responds to one of the six wavelength
bands considered, i. e., the albedo is spectrally uncorrelated. The variances, i. e., the diagonal elements, are set to $\varsigma^2 = 1\mathrm{e}{-6}$.
This is four orders of magnitude smaller than the variance in the first step because the second retrieval step only serves to
235   correct errors in the pre-retrieved surface albedo resulting from the Lambertian surface assumption.

The total a priori covariance matrix results from the composition of the individual matrices responsible for r_g, σ_g, and the
albedo a:

$$\mathbf{S_a} = \begin{bmatrix} \mathbf{S_a}^{r_\mathrm{g}} & \mathbf{0} & \mathbf{0} \\ \mathbf{0} & \mathbf{S_a}^{\sigma_\mathrm{g}} & \mathbf{0} \\ \mathbf{0} & \mathbf{0} & \mathbf{S_a}^{a} \end{bmatrix}. \tag{10}$$

The zero sub-matrices $\mathbf{0}$ are of appropriate sizes to provide no correlation between the retrieval parameters.

240   The noise covariance matrix is assumed to be diagonal, i. e., the noise is spectrally and spatially uncorrelated. Its diago-
nal elements contain the signal-to-noise ratios, which are estimated from the SCIAMACHY measurements. A second order
polynomial is fitted to the radiances of each considered wavelength band and the noise level is calculated from the fit residuals.

The vertical pressure and temperature profiles prevailing at the location and time of each SCIAMACHY observation are
based on ERA-Interim reanalysis produced by the European Centre for Medium-Range Weather Forecasts (ECMWF).

5 Reference aerosol products

The evaluation of the SCIAMACHY v2.0 aerosol retrieval is based on data sets from balloon-borne measurements, as well as SAGE II, SAGE III-M3M, and OSIRIS observations. The instruments and retrieval approaches are briefly introduced below.

5.1 Optical particle counter measurements

Deshler et al. (2003, 2019) provide a long-term record of vertical PSD profiles above Laramie, Wyoming (41°N, 106°W). The PSD profiles cover the altitude range from 15 to 33 km with a vertical sampling of 0.5 km. The data are publicly available at Deshler (2023). They were obtained by balloon-borne optical particle counters (OPCs). The measurement time series began in 1971, and over time, the instruments, calibration factors, and the approach retrieving the PSDs have been improved (Kovilakam and Deshler, 2015; Deshler et al., 2019). The data recorded during SCIAMACHY's operational period were mainly provided by the OPC device based on 40° scattering geometry and a flow rate of 10 L/min. The number of particles is measured in 12 size classes. The instrument itself is only sensitive to particles in a size range between 0.15 and 10.0 μm. Smaller particles with a size of more than 0.01 μm are first enlarged to the optical detection threshold by a connected supersaturation chamber before the total number density is recorded by a second OPC. The measurements are subsequently fitted by either a unimodal (Eq. (1)) or bimodal lognormal size distribution by minimizing the root mean squared logarithmic difference between the fit-function and bin-sized number density measurements (Deshler et al., 2003). The unimodal PSDs are used for comparison with SCIAMACHY-retrieved aerosol characteristics.

5.2 SAGE II

The Stratospheric Aerosol and Gas Experiment II (SAGE II) instrument operated aboard the Earth Radiation Budget Satellite (ERBS) between October 1984 and August 2005. It was launched on 5 October 1984 into a 57° inclination orbit at an altitude of 610 km.

SAGE II measured the solar irradiance attenuated by the Earth's atmosphere at each sunset and sunrise encountered by the instrument using the solar occultation technique. While the instrument was moving, the measurements were performed at different tangent altitudes ranging from cloud top to around 60 km with a vertical resolution of 0.5 km and a horizontal resolution of 2.5 x 200 km². The irradiance was measured in seven channels with center wavelengths between 385 and 1020 nm and bandwidths between 2 and 20 nm.

Determined by the satellite orbit and observation technique, SAGE II provided about 30 irradiance profiles per day, evenly distributed every 24° longitude with a gradual change in the latitude between 80°N – 80°S. Further information about the instrument is provided in, e. g., Mauldin III et al. (1985) and McCormick (1987).

The aerosol extinction coefficients and effective radii retrieved from sunset measurements by the SAGE II version 7.0 algorithm are used for the comparison. The algorithm developed by NASA (National Aeronautics and Space Administration; Damadeo et al., 2013) converts the spectral sun-normalized observations into optical depth profiles for individual trace gases

and aerosols. From those, the vertical profiles of gas concentrations and aerosol extinction coefficients at 386, 452, 525 and 1020 nm are calculated using an onion-peeling technique.

The retrieval of the effective radius is described in Thomason et al. (2008, Method 1) with additional explanations in Kovilakam and Deshler (2015) and Reeves et al. (2008). The effective radius is calculated by assuming an aerosol composition of two different aerosol particle sizes with a total number density of $20\,\text{cm}^{-3}$. From that composition, the minimum and maximum values of the surface area density and the aerosol volume density are derived using the 525 and 1020 nm extinction coefficients. The means of minimum and maximum values are then used to calculate the effective radius according to Eq. (2).

In addition to the effective radii provided in the SAGE II version 7.0 data set, we also retrieve the effective radius based on a dual-wavelength extinction (DWE) ratio. The DWE approach is based on a method described in Yue and Deepak (1983). For that, a unimodal lognormal size distribution with $\sigma_\text{g} = 1.5$ is assumed. The median radius is retrieved by comparing the 525 to 1020-nm extinction ratios from SAGE II version 7.0 with a lookup table consisting of extinction ratios calculated for the same wavelengths using Mie routines (Oxford University, 2022). By using the extinction ratio, the unknown number density cancels out from the retrieval which can subsequently be calculated from the retrieved median radius, the assumed geometric standard deviation, and the extinction coefficient (Eq. (4)). The effective radius is then calculated using Eq. (3).

We chose the extinction coefficients at 525 and 1020 nm because they have the lowest uncertainties of the four available extinction coefficients over almost all altitude levels. Additionally, this selection allows to retrieve a unique median radius in the largest possible radius range. At other wavelengths, Mie resonances may result in extinction ratios yielding multiple possible median radius solutions, especially for median radii larger than roughly 0.425 μm.

The Mie calculations are performed for spherical droplets consisting of 75 % sulphuric acid and 25 % water. The real refractive index is taken from Palmer and Williams (1975), corrected for temperature using Lorentz-Lorenz-corrections as described by Steele and Hamill (1981). The imaginary refractive index is set to zero, i. e., no absorption.

5.3 SAGE III-M3M

The Stratospheric Aerosol and Gas Experiment III (SAGE III) was operational on the Russian Meteor-3M (M3M) satellite from 2002 to 2005. The spacecraft was launched on 10 December 2001 into a sun-synchronous orbit at an altitude of 1020 km with an inclination of 99.5 ° and an ascending node equatorial crossing time of 9:15 am (Roberts et al., 1996).

The SAGE III-M3M instrument performed solar occultation measurements from 0.5 to 100 km altitude. The solar irradiance was measured by a grating spectrometer at 87 wavelengths from 280 to 1550 nm with a spectral resolution of 1.2 nm ($\lambda <$ 1040 nm) or a bandwidth of 30 nm ($\lambda = 1550$ nm). A horizontal slit limited the field of view at the tangent height location to 0.7 km in the vertical and to 1.5 km in the horizontal direction. The orbit of the satellite resulted in sunrise measurements being confined within roughly 60 °S and 35 °S and sunset measurements happening roughly between 40 °N and 80 °N (McCormick and Chu, 2004; Thomason et al., 2010).

The SAGE III version 4.0 algorithm provides aerosol extinction coefficient profiles at nine wavelengths between 384 and 1544 nm at 90 altitude levels from the Earth's surface to an altitude of 45 km (Thomason et al., 2010). The algorithm for processing the measurements works similarly to the SAGE II version 7.0 algorithm.

The PSD parameters are retrieved by a method similar to the SAGE II DWE approach described above. For that, SAGE III
version 4.0 extinction ratios are compared with those from a lookup table calculated by Mie theory. However, due to the
broad wavelength range covered by the nine available wavelengths, the use of extinction coefficients at three wavelengths is
feasible. Two sets of extinction ratios, namely 449 to 756-nm and 1544 to 756-nm, are used instead of only one, creating a
two-dimensional field of median radii and geometric standard deviations for combinations of the two extinction ratios. Thus,
the geometric standard deviation does not have to be assumed, but can instead be retrieved simultaneously with the median
radius. The effective radius is then calculated from Eq. (3). The method has already been successfully applied to SAGE III
measurements aboard the International Space Station (ISS) and is described in detail in Wrana et al. (2021). In analogy to the
DWE algorithm, it is referred to as the triple-wavelength extinction (TWE) ratio approach in the following.

5.4 OSIRIS version 7.2

The Optical Spectrograph and InfraRed Imager System (OSIRIS) operates aboard the Odin satellite. It was launched on 20
February 2001 into a sun-synchronous orbit at an altitude of 610 km with a local descending node equator crossing time of
6 am. OSIRIS has been measuring the scattered radiance of the terrestrial limb since November 2001.

The relevant data comes from the optical spectrograph. It is a grating spectrometer that covers the wavelength range from
280 to 810 nm with a spectral resolution of about 1 nm. The horizontal slit in the entrance optics limits the field of view at the
limb tangent height to 40 km in the horizontal and to 1 km in the vertical direction. By continuously tilting the entire satellite,
OSIRIS scans the limb from 7 km to 75 km with a sampling interval of about 2 km, depending on the measurement integration
time. One profile scan takes about 40 seconds and covers approximately 400 km along the satellite track at the ground. Sunlit
observations in the mid and high latitudes are not available in the winter hemisphere. Global coverage from 82 °N to 82 °S is
only achieved in spring and autumn. Further information about the instrument is provided in Warshaw et al. (1996), Llewellyn
et al. (2004), and McLinden et al. (2012).

This paper uses the OSIRIS version 7.2 aerosol extinction coefficients at 750 nm (Rieger et al., 2019). The algorithm is a
multi-wavelength retrieval assuming a fixed unimodal lognormal PSD with $r_\mathrm{g} = 0.08\,\mu$m and $\sigma_\mathrm{g} = 1.6$. During the iterative
procedure, the number density is retrieved and converted to the extinction coefficient using the assumed particle size. The
measurement vector contains reference-height-normalized limb measurements. These are additionally normalized by radiances
of a variable wavelength combination to reduce noise and decrease sensitivity to the PSD assumptions.

6 Sensitivity tests

The retrieval of the aerosol PSD parameters r_g and σ_g from SCIAMACHY observations described in Sect. 4 is based on two
assumptions. First, the surface is assumed to be Lambertian. Second, the number density profile is fixed at the beginning of the
retrieval and is unalterable. Both assumptions do not have to be correct for any given SCIAMACHY observation. Therefore,
we test the retrieval for its sensitivity to both assumptions using a synthetic measurement set.

Table 1. Selected scenarios of aerosol loads (adapted from Malinina et al. (2018)).

Aerosol load	R_{mod}, μm	r_{g}, μm	σ_{g}	w, μm	SAOD
Small	0.060	0.080	1.700	0.052	0.017
Background	0.080	0.100	1.600	0.055	0.027
Unperturbed	0.110	0.121	1.370	0.041	0.021
Volcanic	0.200	0.207	1.200	0.039	0.130

This synthetic data set has been created by using SCIATRAN (Rozanov et al., 2014; Mei et al., 2023). It contains the nadir and limb radiances for the illumination and observation geometries of one randomly chosen SCIAMACHY orbit. The time of the orbit is irrelevant, just as there is no need for multiple orbits to account for seasonality. The reason lies in the single-scattering angle, the crucial angle of the illumination and observation geometry that affects the quality of the retrieval. Since this angle varies more within an orbit than per year at constant latitude, the seasonal range of the single-scattering angle - and therefore the seasonal dependency of the retrieval - is covered by the variation of the single-scattering angle along an orbit.

The nadir and limb radiances are simulated assuming a vegetated surface. Its anisotropic reflectance is defined by the bidirectional reflectance distribution function (BRDF). The BRDF describes the scattering of the incident irradiance from an infinitesimal solid angle into the infinitesimal solid angle of another direction (Schaepman-Strub et al., 2006). The BRDF is calculated by the Ross-Li semi-empirical model (Lucht et al., 2000) with parameters $f_{\mathrm{iso/vol/geo}} = 0.36/0.24/0.03$. The values are based on the Moderate Resolution Imaging Spectroradiometer (MODIS) MCD43A1 data set over a vegetated surface of Amazonia (Lorente et al., 2018). The simulated surface is characterized by an enhanced backscattering and a lowered forward-scattering reflectance. At a solar zenith angle of $35\,^{\circ}$, the BRDF ranges between 0.09 and 0.12 at VZA of $26\,^{\circ}$ and between 0.10 and 0.11 at VZA of $9\,^{\circ}$. The black-sky albedo, as defined by the albedo of the surface that is illuminated only by the sun without any atmospheric contribution, is 0.33. Larger solar zenith angles entail a higher anisotropy and albedo values.

The simulated atmosphere contains aerosols between 12 and 46 km altitude. Their PSD profiles are specified below. Pressure and temperature profiles as well as the extraterrestrial solar irradiance are chosen in accordance with the randomly selected SCIAMACHY orbit.

6.1 Sensitivity to Lambertian surface assumption

To investigate the influence of the Lambertian surface assumption on the retrieved aerosol PSD parameters, the nadir and limb radiances are simulated with four different aerosol loads: "small", "background", "unperturbed", and "volcanic". The cases are selected similar to Malinina et al. (2018). The PSD paramaters R_{mod}, r_{g}, and σ_{g} are constant with altitude and are summarized in Table 1. In the "unperturbed" case, the PSD parameters are the same as the a priori values. The number density profile is based on balloon-borne measurements over Wyoming (Deshler et al., 2019). The profile is shown later in Fig. 2. This number density profile is also used as a priori in the subsequent retrieval procedure.
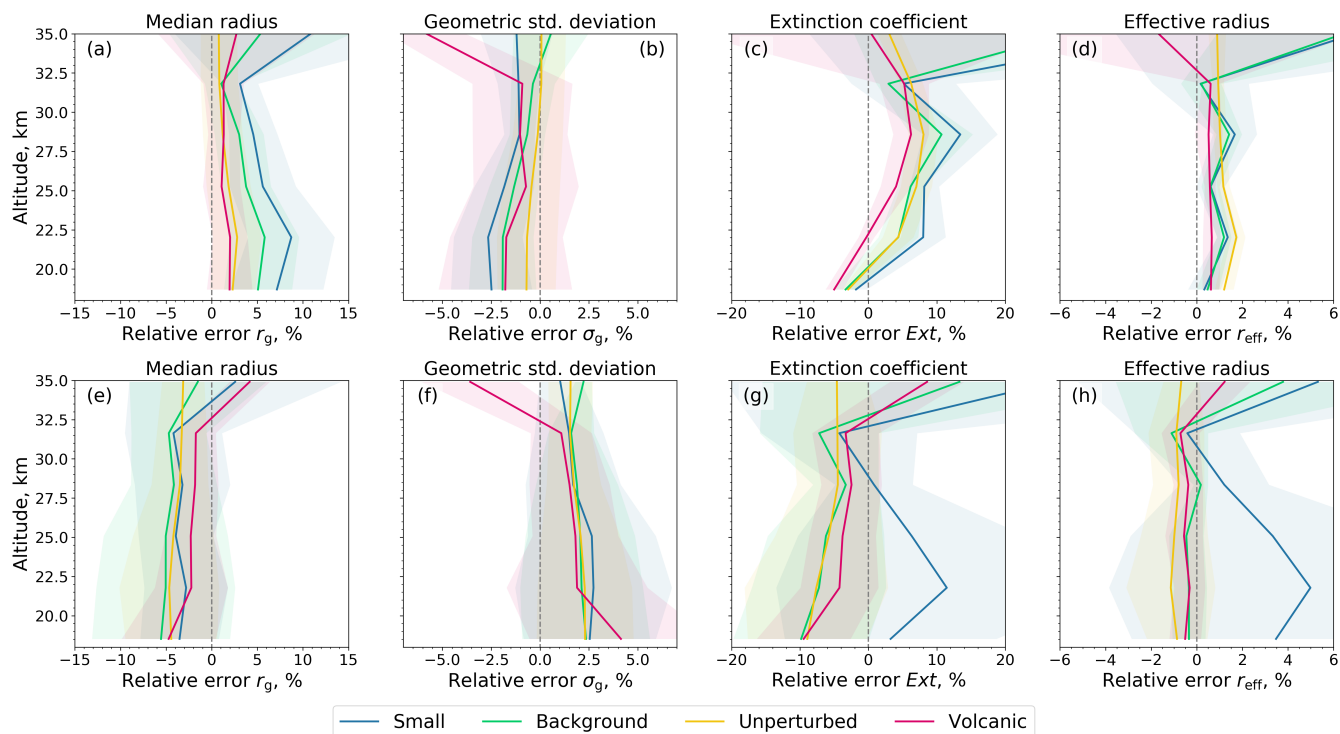
Figure 1. Uncertainties in the retrieved aerosol characteristics due to the Lambertian surface assumption for different artificial aerosol load scenarios given in Tab. 1. Relative errors are calculated as (retrieval - true) / true × 100 %. Solid lines show the relative errors averaged over 12 profiles at the western (a-d) and eastern edge (e-h) of one randomly chosen SCIAMACHY orbit. Shading areas depict their standard deviations.

The simulated nadir radiances are used to derive the effective Lambertian surface albedo. The nadir measurements observing the surface closer to its forward-scattering region slightly underestimate the correct surface albedo while nadir measurements observing the surface closer to its backscattering region overestimate the correct surface albedo. The error increases from VZA of 9 to 26 ° and is almost independent of the aerosol amount.

370   In the second step, the retrieved albedo is used as the a priori Lambertian surface albedo to retrieve r_g and σ_g from simulated limb radiances. Unlike the description in Sect. 4, the albedo retrieval is switched off in this step in order to better investigate the effects of an incorrectly assumed Lambertian surface.

Figure 1 shows the relative mean error between the retrieved and true profile of aerosol characteristics. We averaged the errors along the orbit. Only profiles with single-scattering angles between 20 and 96 ° are taken into account. This corresponds

375   to an orbital segment of 12 limb observation sequences with latitudes north of 26 °N in summer and 23 °S in winter. Limb radiances at single-scattering angles greater than 96 ° are less sensitive to PSD parameters making it difficult to retrieve the PSD parameters separately.

The upper panel of Fig. 1 contains the mean error of profiles at the western edge of the swath, while the lower panels contains the mean error of profiles at the eastern edge of the swath. We selected the profiles at the edges of the swath as corresponding

380   nadir measurements have VZAs of $\pm 26\,°$. For those limb profiles, the errors in the a priori surface albedo are the largest and thus have the strongest influence on the PSD retrieval.

At the western edge of the swath, the corresponding nadir observations are from the near forward-scattering region of the surface, where surface reflectances are lower than the surface albedo. The retrieved effective Lambertian surface albedo is therefore underestimated. Using this underestimated value as the a priori Lambertian surface albedo in the PSD retrieval leads

385   to a mean overestimation of r_g by up to 11.2 % and a mean underestimation of σ_g by mostly up to 2.7 %. Vice versa, nadir observations at the eastern edge of the swath are from the near backscattering region of the surface, where surface reflectances are larger than the surface albedo. The retrieved surface albedo is therefore overestimated, resulting in a mean underestimation of r_g by up to 5.6 % and a mean overestimation of σ_g by up to 4.1 %. The errors in the retrieved PSD parameters result in an error of mostly less than ± 13.4 % in Ext and ± 5 % in r_eff.

390   It is worth emphasizing that strongly anisotropic surfaces not only cause a bias in the aerosol characteristics. They also induce a slope of the bias in the across-track direction. However, it is assumed that for real measurements, the upwelling radiance scattered into the instrument's field of view originates from different anisotropic surface types. The integration of these radiances likely smooth out the anisotropic reflectance contribution of each individual surface type, resembling a Lambertian surface. This reduces the impact of the Lambertian surface assumption on the PSD parameter retrieval.

395   ## 6.2 Sensitivity to aerosol number density

We repeat the simulation of nadir and limb radiances by assuming altitude-dependent profiles of r_g, σ_g, and N. The profiles are based on balloon-borne measurements over Wyoming (Deshler et al., 2019) and are shown in Fig. 2 as black lines. The PSD parameters r_g and σ_g are retrieved using different a priori N profiles. Note that the albedo is also retrieved in the second step of the retrieval algorithm as described in Sect. 4. The obtained PSD is used to calculate Ext and r_eff by Eqs. (4) and (3).

400   Figure 2 shows the resulting profiles of r_g, σ_g, Ext, and r_eff using the correct N profile (red), halving (yellow) or doubling (green) the correct N profile, or using a N profile with a modified shape (blue) as a priori in the retrieval procedure. The latter profile is based on the ECSTRA model climatology for aerosol background conditions (Fussen and Bingen, 1999).

The results are averaged over all profiles of the randomly chosen SCIAMACHY orbit within an orbital segment of single-scattering angles between 20 and $96\,°$. Since this orbital segment comprises 12 limb observation sequences of 4 profiles each,

405   48 profiles are considered in the averaging. The biases in the retrieved (r_g, σ_g) and calculated data (Ext, r_eff) are mainly due to the biases in the a priori N profile and the uncertainties in the retrieval algorithm itself. Their standard deviations are mainly due to the assumption of a Lambertian surface.

If the correct N profile is used as a priori, errors in r_g, σ_g, and r_eff are mostly smaller than 9.5 %, 0.7 %, and 9.2 %, respectively. Errors in Ext can exceed 20 % but are explainable by the small absolute extinction coefficients. A larger assumed

410   N profile leads to wider PSDs with smaller aerosols in the logarithmic space, a smaller assumed N profile leads to narrower
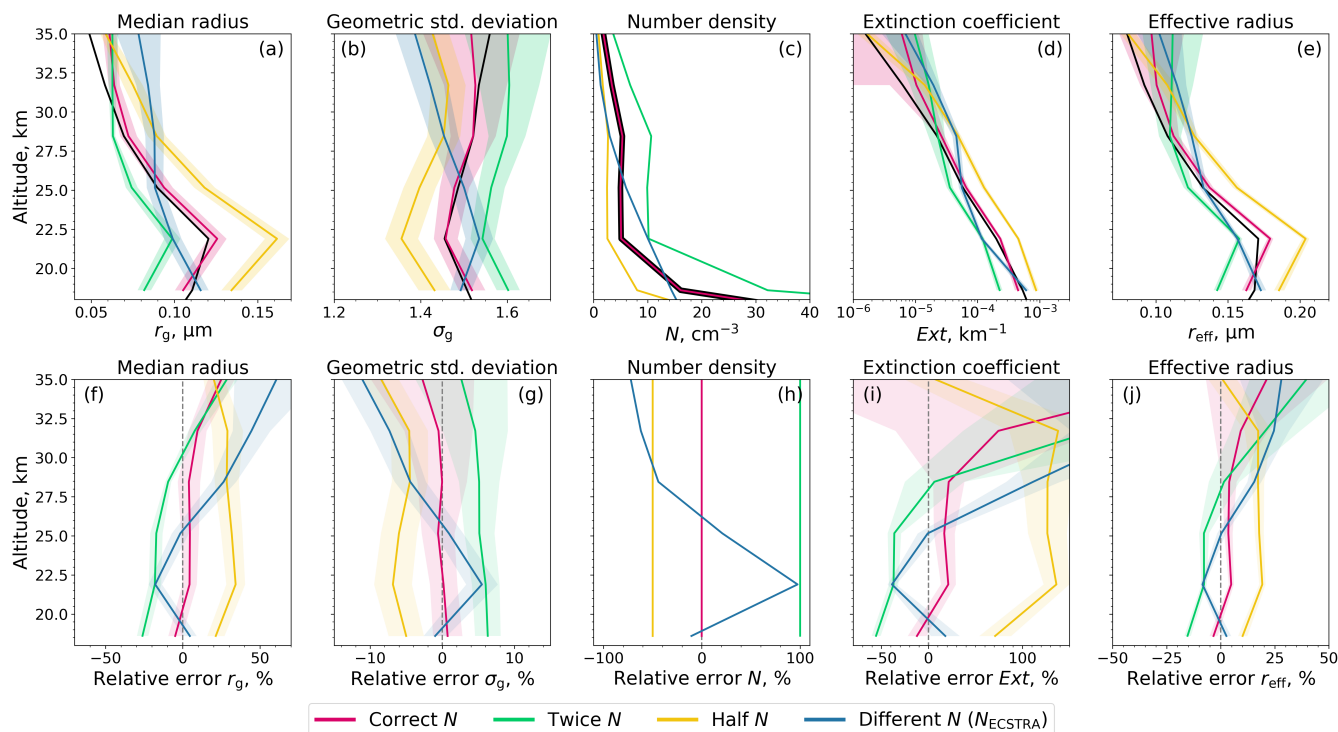
Figure 2. Profiles of the aerosol characteristics (a-e) and their relative errors (f-j). Black: true artificial aerosol load scenario. Colours: retrievals using a correct (red), twice as high (green), half as high (yellow), and differently shaped (blue) number density profile as a priori. Relative errors are calculated as (retrieval - true) / true × 100 %. Solid lines are averages over 48 profiles of one randomly chosen SCIAMACHY orbit, shading areas depict their standard deviations.

PSDs with larger aerosols. If the shape of the a priori N profile also changes, the shapes of the aerosol characteristic profiles differ from the correct ones, especially in case of r_g and σ_g.

To conclude, the correct selection of the a priori N is crucial for the accurate retrieval of r_g and σ_g as well as for the subsequent calculation of Ext and r_eff. However, the spatio-temporal distribution of the stratospheric N is essentially unknown in reality. The SCIAMACHY retrieval has to rely on assumptions here that lead to errors in the retrieved and calculated aerosol characteristics.

Note that this sensitivity study does not consider profiles with single-scattering angles greater than 96 °, which correspond to profiles at latitudes south of 26 °N in summer and 23 °S in winter. Radiances from single-scattering angles greater than 96 ° are less sensitive to aerosols due to much smaller phase function values (Rieger et al., 2014, 2019). This limits the separate retrieval of r_g and σ_g from the measured signal. However, in Sect. 7 it is shown that even for the entire southern hemisphere, Ext and r_eff calculated from r_g and σ_g give reasonable results.
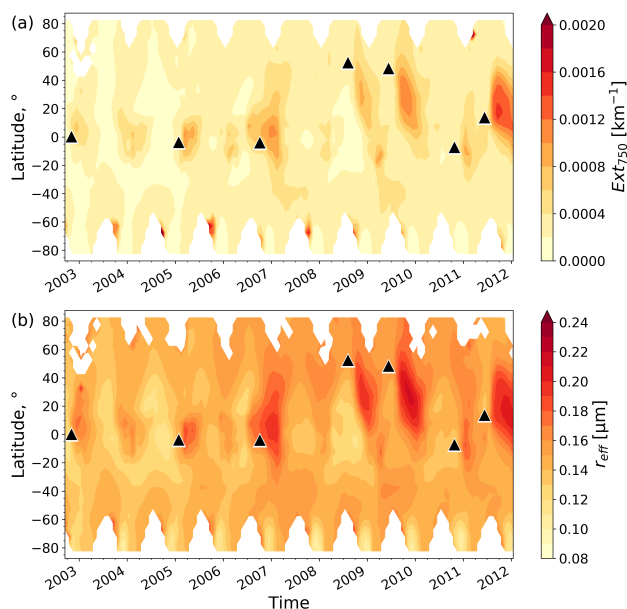
Figure 3. Temporal evolution of the aerosol extinction coefficient at 750 nm (a) and of the aerosol effective radius (b) at 18.4 km altitude, derived from SCIAMACHY measurements (v2.0 data set) between August 2002 and December 2011. Aerosol extinction coefficients greater than $0.1 \, \text{km}^{-1}$ are excluded. Black triangles indicate major volcanic eruptions.

7 Evaluation

The median radius and geometric standard deviation profiles are retrieved for the SCIAMACHY observation period between 2002 and 2011. From these, extinction and effective radius profiles are calculated. The results at 18.4 km altitude are presented in Fig. 3. The temporal development of stratospheric aerosols during post-volcanic periods is dominated spatially by advection and microscopically by nucleation, coagulation, condensation, and sedimentation and these processes are evidenced in Fig. 3.

The SCIAMACHY v2.0 retrieved $(r_{\text{g}}, \sigma_{\text{g}})$ and calculated aerosol characteristics (Ext, r_{eff}) are evaluated with aerosol products obtained from balloon-borne measurements and satellite observations. The comparison of aerosol extinction coefficients is performed at 750 nm, where a direct comparison with the OSIRIS and our previous SCIAMACHY v1.4 Ext is possible. Therefore, the SAGE II and SAGE III extinction coefficients are converted to 750 nm via the Ångstrom exponent (Eq. (5)) calculated for the extinction ratio of 525 to 1020 nm and 520 to 1021 nm, respectively. The aerosol extinction from balloon-borne measurements is calculated by using Eq. (4)

7.1 Comparison with balloon-borne measurements

The comparison of SCIAMACHY aerosol observations and balloon-borne measurements includes 23 collocated profiles over Wyoming between 2003 and 2012 with a maximum distance of 750 km and a maximum time mismatch of 12 hours. The
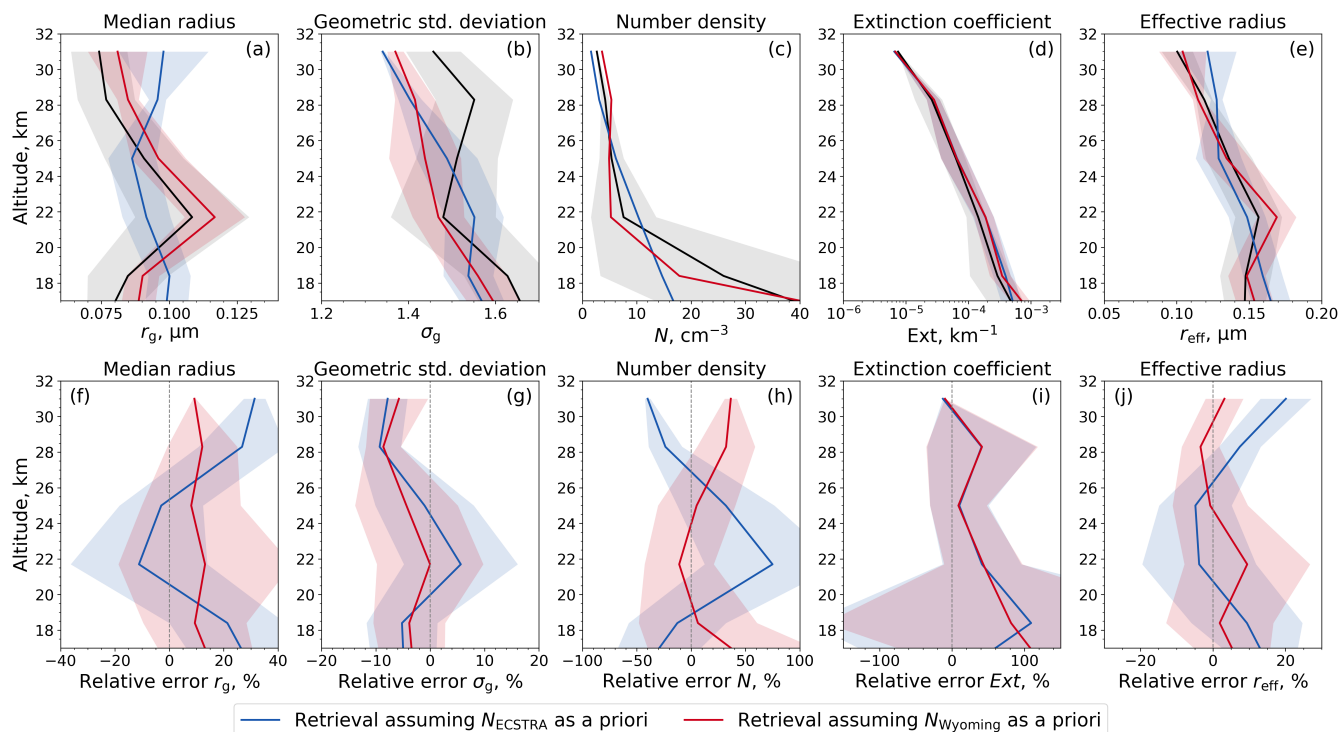
Figure 4. Comparison of balloon-borne-measured and SCIAMACHY-observed aerosol characteristics over Laramie, Wyoming, USA, between 2003 and 2012 (from left to right: median radius, geometric standard deviation, number density, extinction coefficient at 750 nm, effective radius). Absolute values (a-e) and relative errors (f-j) are averaged over 23 profiles with $r_\mathrm{g} > 0.06\,\mu\mathrm{m}$ (lines). Shading areas depict their standard deviations. Relative errors are calculated as (SCIAMACHY - balloon)/balloon × 100 %. Black: Balloon-borne measurements. Blue, red: SCIAMACHY observations assuming a priori number densities shown in panel (c).

profiles are distributed over all seasons. Balloon-borne measurements are smoothed by a moving average, using a boxcar function of 3 km width, and subsequently interpolated onto the SCIAMACHY vertical grid.

Figure 4 compares the retrieved profiles of the median radius (a) and the geometric standard deviation (b) as well as the calculated profiles of the extinction coefficient at 750 nm (d), and the effective radius (e) from SCIAMACHY with the data

440 obtained from balloon-borne measurements. Two a priori number density profiles are assumed for the retrieval of aerosol characteristics, one based on the ECSTRA model climatology (Fussen and Bingen, 1999, Fig. 4(c) - blue) and one based on balloon-borne measurements over Wyoming before 2002 (Fig. 4(c) - red). Since SCIAMACHY is not sensitive to stratospheric aerosols with $r_\mathrm{g} < 0.06\,\mu\mathrm{m}$ (Malinina et al., 2019), corresponding OPC PSDs are excluded from the comparison.

The relative errors of r_g and σ_g are mostly below 26.8 % and 9.3 %, respectively (Fig. 4(f-g)). The smaller the error in the

445 a priori N profile, the smaller the retrieval errors. A more accurate a priori N profile can usually improve the accuracy by more than a factor of 2. Furthermore, r_g and σ_g are highly anti-correlated: If r_g is underestimated, σ_g is overestimated and vice versa. This relation leads to a more accurate estimation of r_eff (Fig. 4(e)) and reduces their maximum relative deviations

mostly down to 9.4 % (Fig. 4(j)). Relative errors in Ext can exceed 100 %, which can be explained by a small reference value (Fig. 4(i)).

450   The benefit of evaluating the aerosol characteristics obtained by SCIAMACHY with in-situ balloon-borne measurements is limited by the fact that the latter come from only one measurement site. There are also some balloon-borne measurements over Kiruna, Sweden, but at the times of OPC measurements, SCIAMACHY observations are sparse: Only 3 collocations of balloon-borne measurements with SCIAMACHY observations with distances of up to 3000 km are available. Due to the small amount of data, a comparison of aerosol characteristics over Kiruna is not carried out. Instead, satellite data is used for a global
455   evaluation.

7.2 Comparison with SAGE II, SAGE III, and OSIRIS

To compare the aerosol characteristics from SCIAMACHY with those from SAGE II, SAGE III-M3M, and OSIRIS, the SCIAMACHY profiles are collocated with each of the other satellite instruments. In case of SAGE III and OSIRIS, a maximum distance of 200 km is used. In case of SAGE II, the maximum distance is increased to 500 km to obtain a sufficient number of
460   collocations. The maximum collocation time offset is 12 h. A total number of 4255 coincident profiles from the years 2002 to 2005 are available for the comparison of SCIAMACHY with SAGE II data. For the SAGE III - SCIAMACHY comparison, there are 5909 collocated profiles for the same time period. For the OSIRIS - SCIAMACHY comparison, almost 200,000 coincident profiles are available from 2002 to 2012.

All data with an extinction coefficient greater than $0.1\,\mathrm{km^{-1}}$ are excluded from the comparison to reduce cloud effects.
465   As the measurements of OSIRIS and both SAGE instruments provide a higher vertical resolution than SCIAMACHY, they are smoothed by a moving average, using a boxcar function of 3 km width as a weighting function, and are subsequently interpolated onto the SCIAMACHY vertical grid.

Figure 5 compares the extinction coefficient profiles from SAGE II, SAGE III, and OSIRIS to those from SCIAMACHY. The differences are averaged over specified latitudinal bins. Due to the inclination of the Meteor-3M orbit, the SAGE III profiles
470   are asymmetrically distributed over the northern and southern hemisphere and there are no profiles over the tropics.

The extinction coefficients from SCIAMACHY and SAGE II, SAGE III, or OSIRIS mostly agree within 30 %. Discrepancies are slightly higher in the tropics at altitudes below 22 km due to cloud effects, and at altitudes above 28 km due to smaller absolute values. SCIAMACHY Ext is mostly smaller than that from OSIRIS, while the sign of differences between SCIAMACHY and both SAGE data series depends on the latitude.

475   In addition to the SCIAMACHY v2.0 product, we also included the SCIAMACHY v1.4 Ext (Rieger et al., 2018) in the comparison. In contrast to Ext v2.0, Ext v1.4 is retrieved directly from the SCIAMACHY radiances at 750 nm that are normalized to measurements at the reference tangent altitude of 38 km. During the retrieval, a fixed unimodal lognormal PSD with $r_\mathrm{g} = 0.08\,\mu\mathrm{m}$ and $\sigma_\mathrm{g} = 1.6$ is assumed. The retrieval algorithm is described in detail in von Savigny et al. (2015) and Rieger et al. (2018).

480   It can be seen from Fig. 5 that in the northern hemisphere the difference in Ext between SCIAMACHY v2.0 and v1.4 is about -10 % and is comparable to the difference in Ext between SCIAMACHY v2.0 and other satellite instruments. In the
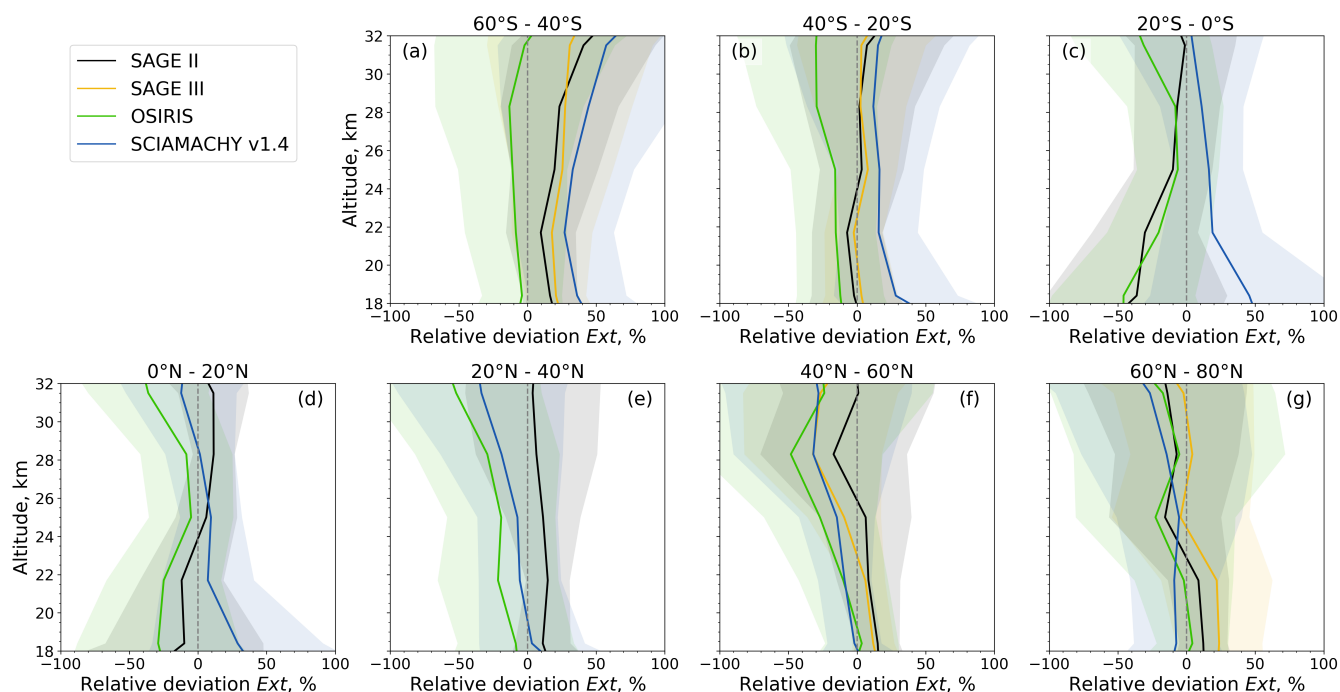
Figure 5. Comparison of extinction coefficients at 750 nm from SCIAMACHY v2.0 data with those from SAGE II, SAGE III-M3M, OSIRIS, and SCIAMACHY v1.4. Relative deviations are calculated as (SCIAMACHY v2.0 - Instrument) / (SCIAMACHY v2.0 + Instrument) × 200 %. Solid lines show the averages within indicated latitudinal bins, shading areas depict the standard deviations.

southern hemisphere, however, Ext v2.0 can be on average more than 50 % larger than Ext v1.4. Due to the good agreement of SCIAMACHY v2.0 Ext with the SAGE II, SAGE III, and OSIRIS products, we conclude that SCIAMACHY v1.4 highly underestimates Ext in southern latitudes while the new algorithm version provides more accurate Ext values.

485   In addition to the improved extinction coefficient, SCIAMACHY v2.0 also provides effective radii that can be compared to those of the SAGE series data as shown in Fig. 6. In case of SAGE II, two different r_{eff} products, one retrieved with the SAGE II v7.0 algorithm from NASA (Damadeo et al., 2013) and one retrieved with the DWE approach described in Sect. 5.2, are compared to r_{eff} from SCIAMACHY. In case of SAGE III, r_{eff} is retrieved with the TWE approach (Wrana et al., 2021).

     The effective radii from SCIAMACHY are systematically lower than those from SAGE II and SAGE III, with the differences 490   decreasing with altitude. Best agreement is achieved between SCIAMACHY and SAGE III with deviations of 1.3 to 17.9 %. The differences of r_{eff} between SCIAMACHY and SAGE II can increase up to 45.6 % (v7.0 NASA) and 57.0 % (DWE).

     Missing (in case of SAGE III) or highly variable (in case of SAGE II) effective radii at higher altitudes are artefacts of the DWE and TWE approaches. These altitudes are characterized by a typically low aerosol content that leads to low signal-to-noise ratios in the satellite measurements and thus to noisy extinction ratios. Using two of them in the SAGE III TWE approach 495   reduces the likelihood of a successful retrieval of the effective radius. In contrast, the SAGE II DWE approach requires only one extinction ratio. Though this fact increases the probability of a successful retrieval of the effective radius it is associated
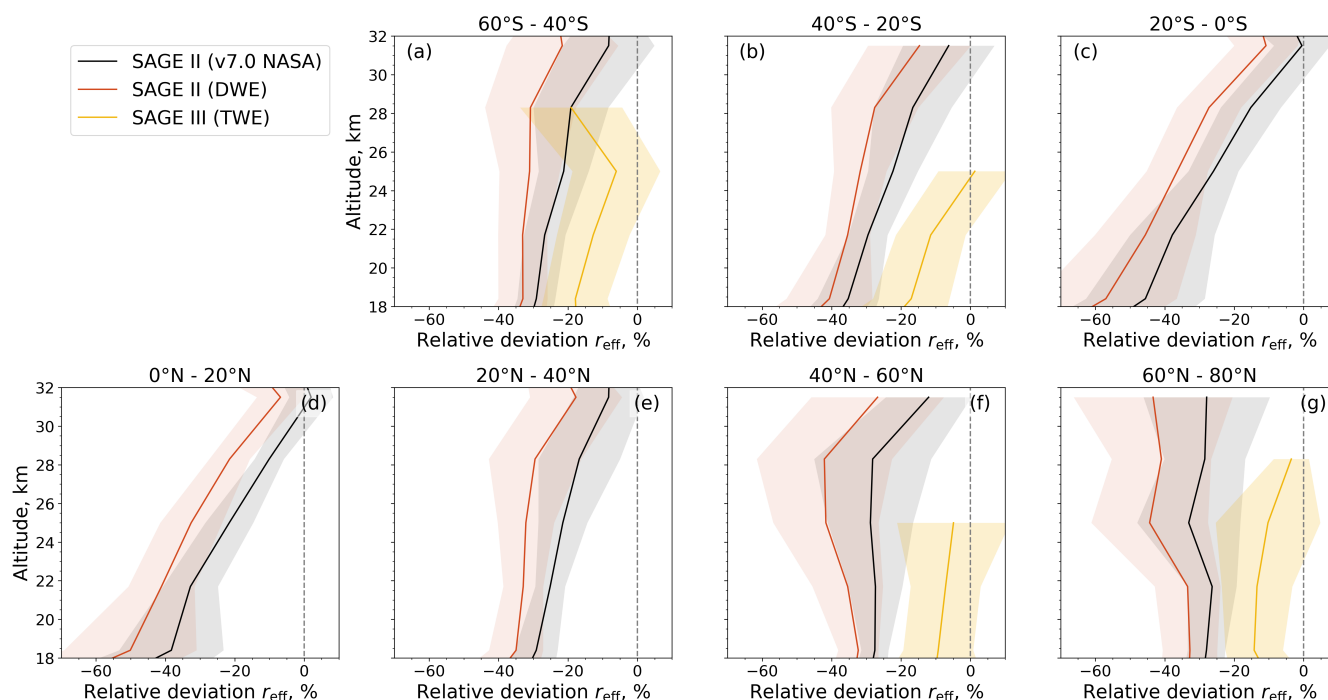
Figure 6. Comparison of effective radii from SCIAMACHY v2.0 with those from SAGE II and SAGE III-M3M. Relative deviations are calculated as (SCIAMACHY v2.0 - Instrument) / (SCIAMACHY v2.0 + Instrument) × 200 %. Solid lines show the averages within indicated latitudinal bins, shading areas depict the standard deviations.

with large uncertainties. High clouds in the tropics also provide large variability in the effective radius at the altitudes below 22 km albeit to a much smaller extent than for the extinction coefficient (Fig. 5).

In principle, both the DWE and TWE approach provide PSDs from SAGE observations that can be compared with those

500   retrieved from SCIAMACHY observations. However, SCIAMACHY v2.0 and the SAGE II DWE approach rely on different assumptions, the former utilizes a fixed number density profile whereas the latter uses a fixed geometric standard deviation. These assumptions have a significant impact on the PSD shape finally retrieved. Therefore, a comparison of SCIAMACHY and SAGE II-retrieved PSDs is more an evidence of the (in)correctly assumed parameters than an evaluation of the SCIAMACHY PSD product per se. Therefore, we limit ourselves to the comparison of PSD data retrieved from SCIAMACHY v2.0 and the

505   SAGE III TWE approach (Fig. 7). The comparison is further limited to the latitude bins 40 - 60 °N and 60 - 80 °N due to the restricted global distribution of SAGE III observations (Sect. 5.3) and the limitation of the separate retrieval of r_{g} and σ_{g} to the northern hemisphere (Sect. 6.2).

Figure 7 shows differences in r_{g} and σ_{g} between SCIAMACHY and SAGE III of less than 26.5 % and 10.5 %, respectively. The error in the a priori N can be by up to 51.1 %. Analogous to the comparison with balloon data (Sect. 7.1), the differences

510   in r_{g} and σ_{g} correlate with the differences between SCIAMACHY-assumed and SAGE III-retrieved number densities.
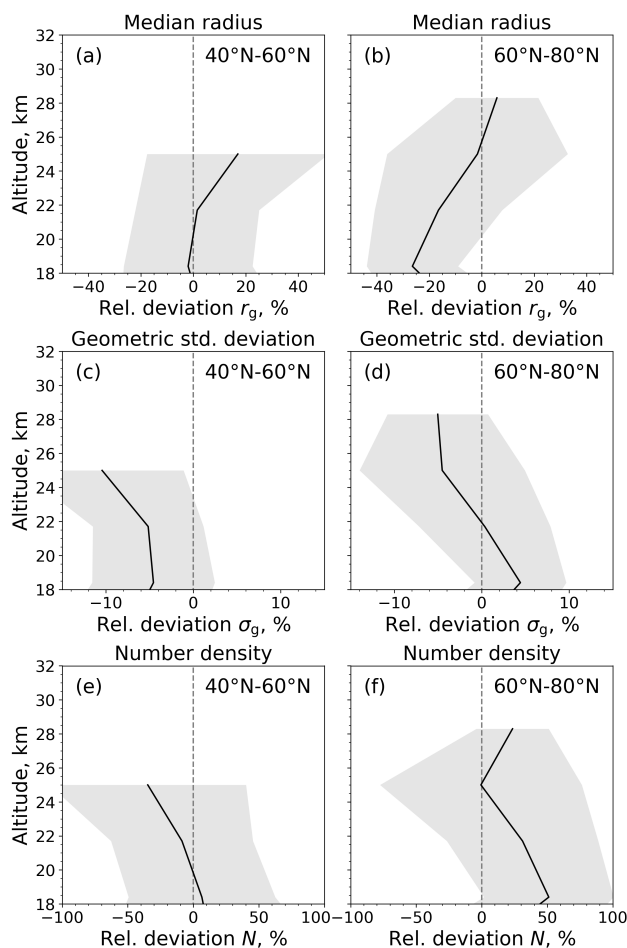
Figure 7. Comparison of aerosol PSD parameters from SCIAMACHY and SAGE III-M3M (from top to bottom: median radius, geometric standard deviation, number density). Relative deviations are calculated as (SCIAMACHY - SAGE)/(SCIAMACHY + SAGE) × 200 %. Solid lines show the averages in the latitudinal range of 40 - 60 °N (a,c,e) and 60 - 80 °N (b,d,f). Shading areas depict the standard deviations.

7.3 Temporal comparison

The temporal evolution of the extinction coefficient and the effective radius between 1989 an 2012 is presented in Fig. 8 using the collocations of SAGE II and OPC (crosses), SCIAMACHY and OSIRIS (lines), SCIAMACHY and OPC (stars), SCIA-MACHY and SAGE II (filled circles), as well as SCIAMACHY and SAGE III (triangles). The altitude of 21.7 km was chosen

515 arbitrarily. The data from the intersatellite comparison are presented as monthly averages, in the case of the SCIAMACHY-OSIRIS comparison two-month averages, within the latitude range of 40 °-60 °N. OPC and collocated satellite data are single values. The high resolution profiles of OPC, SAGE II, SAGE III, and OSIRIS are smoothed by a moving average, using a box-
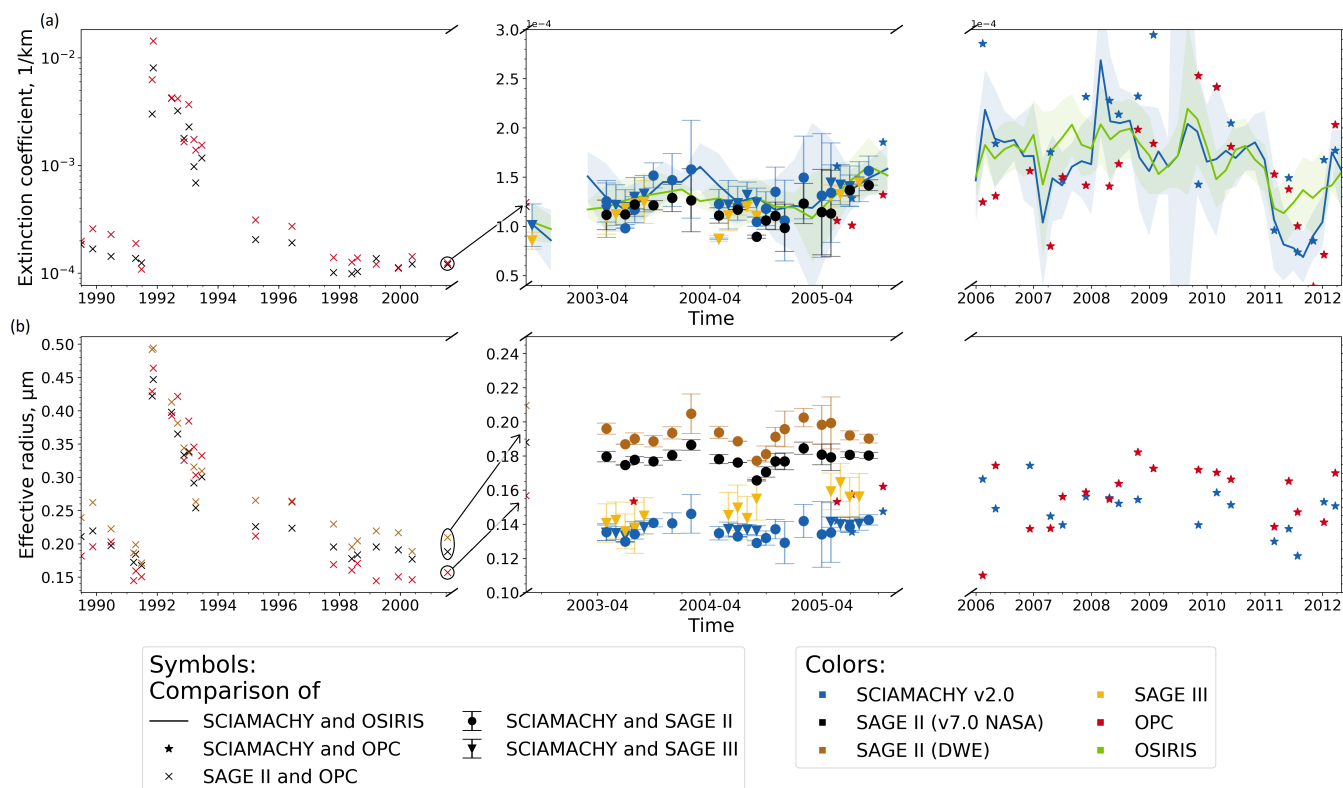
Figure 8. Time series of extinction coefficients (a) and effective radii (b) at 21.7 km between 40 ° - 60 °N. SCIAMACHY is compared to OSIRIS (lines), OPC (stars), SAGE II (filled circles), and SAGE III-M3M (triangles). SAGE II is compared to OPC (crosses). Intersatellite comparisons are monthly (filled circles, triangles) or two-months means (lines) with standard deviations (bars, shading areas). Comparisons with OPC data are instantaneous measurements (crosses, stars). Note the changes in parameter scales between the single figure panels.

car function of 3 km width, and are subsequently interpolated onto the SCIAMACHY vertical grid. Note that for illustration purposes, the scales of time and aerosol characteristics are adjusted in the individual figure panels.

520   All products show a temporally synchronous development of the extinction coefficient (Fig. 8(a)), which increases after volcanic eruptions such as Pinatubo (Jun 1991), Reventador (Nov 2002), Manam (Jan 2005), Kasatochi (Aug 2008), Sarychev (Jun 2009), and Nabro (Jun 2011). As already shown in Figs. 4-5, SCIAMACHY has on average slightly larger extinction coefficients than SAGE II, SAGE III, and OPC, while SCIAMACHY and OSIRIS agree on average. Although extinction coefficients from SAGE II and III are not directly comparable, as their mapped profiles are from different locations and times,

525   their temporal trajectories indicate an agreement of both products.

    In contrast to the matching extinction coefficients, the effective radius products exhibit a two-track behaviour (Fig. 8(b)). The effective radii of both SAGE II algorithms agree well with only a minor offset of 0.015 μm. The effective radii of SCIAMACHY and SAGE III are also similar, at least until July 2004. However, both SAGE II products are 0.04-0.05 μm larger than the

effective radius from SCIAMACHY and SAGE III. OPC measurements - and SAGE III observations since August 2004 - are

530 slightly larger than the effective radius of SCIAMACHY and show a smaller but still significant offset to the SAGE II product, at least during periods of low aerosol loading.

Note that effective radii from SAGE III increase slightly but significantly over time. It is due an increasing median radius with a simultaneously decreasing geometric standard deviation. Such an evolution of the aerosol particle size is not observed in SCIAMACHY and both SAGE II (v7.0 NASA, DWE) data sets. This might be because in those three retrieval algorithms

535 one of the PSD parameters is assumed to be constant.

The temporal development of the effective radius follows that of the extinction coefficient, i. e., the effective radius increases with a larger extinction coefficient and vice versa. The offsets between the r_{eff} products remains nearly constant in time – at least in the period 1999 – 2005. After the Pinatubo eruption 1991, the SAGE II effective radius is similar or even slightly lower than that of the OPC measurements.

8 Discussion

540

The SCIAMACHY version 2.0 algorithm retrieves the median radius and geometric standard deviation in the northern hemisphere and calculates globally the extinction coefficient and the effective radius of aerosols between 18 and 35 km altitude. The extinction coefficient of SCIAMACHY v2.0 agrees better with independent satellite observations than that of the algorithm version 1.4 (Rieger et al., 2018). The temporal development of the effective radius is consistent with the other observations.

545 However, the effective radii from SCIAMACHY v2.0, SAGE II, and SAGE III reveal biases that are most prominent between SCIAMACHY / SAGE III and both SAGE II products (Figs. 6, 8). The cause of the biases remains to be clarified. The accuracy of the retrieved median radius and geometric standard deviation depends on uncertainties in the assumed fixed number density. Uncertainties in both PSD parameters may blow up in case of a disregarded strong increase of the number density, e. g., after volcanic eruptions or biomass burning events. All these topics are discussed in the following.

8.1 Aerosol extinction coefficient improvement

550

Extinction coefficients from SCIAMACHY v2.0 data agree better with independent satellite observations than those of v1.4 (Rieger et al., 2018) for two reasons. Firstly, the v2.0 algorithm normalizes the measured radiances by the extraterrestrial solar irradiance (Eq. (6)) and not by a measurement at an upper tangent height, as in version 1.4. This fact makes the v2.0 aerosol retrieval independent of a variable aerosol situation at the normalization altitude (Rieger et al., 2018). The disadvantage of

555 this approach is a stronger influence of the surface albedo on the retrieval results. However, this effect can be mitigated by the prior determination of the effective surface albedo from nadir measurements. Secondly, the v2.0 algorithm utilizes multiple wavelengths between 748 and 1306 nm to retrieve the aerosol characteristics while version 1.4 utilizes a single wavelength of 750 nm. The multi-wavelength approach stabilizes the retrieval and increases the sensitivity to aerosols (Rieger et al., 2018).
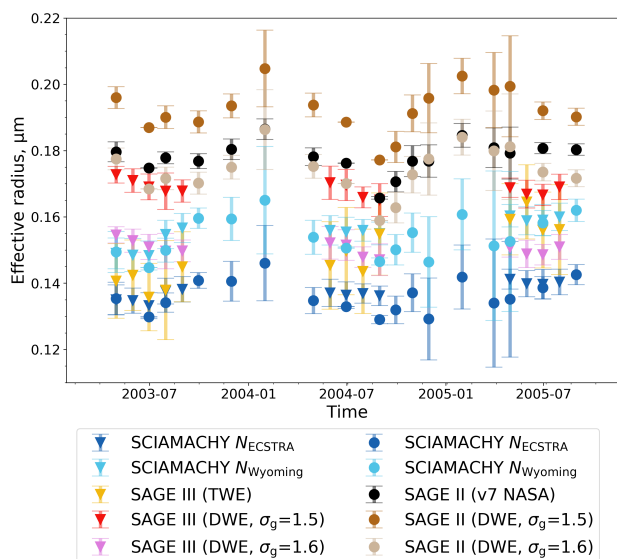
Figure 9. Effective radii same as in Fig. 8(b, middle) but using different a priori conditions and minor algorithm adjustments in the retrieval of effective radii from SCIAMACHY v2.0 (bluish), SAGE II (black, ochreous), and SAGE III-M3M (yellow, reddish).

8.2 Effective radius offset

560 Figure 8(b) presented distinct biases between the effective radii from the different satellite data products. Several reasons may be responsible for these offsets.

8.2.1 A priori assumptions

We tested different a priori conditions and minor algorithm adjustments. The result is exemplified in Fig. 9 at an altitude of 21.7 km. Instead of the number density profile based on the ECSTRA model climatology (blue line in Fig. 2), we used the
565 profile based on balloon-borne measurements over Wyoming (black line in Fig. 2) as a priori in the SCIAMACHY v2.0 aerosol retrieval algorithm. The resulting effective radius at 21.7 km altitude is 0.02 μm larger, but the effect is too small to be solely responsible for the bias between the effective radii of SCIAMACHY and SAGE II.

Next, the a priori geometric standard deviation from the SAGE II DWE approach is increased from 1.5 to 1.6. This results in a 0.02 μm smaller effective radius, which is similar to that from SAGE II v7.0 NASA (Fig. 9).
570 In a third test, we checked the differences between the DWE approach of SAGE II and the TWE approach of SAGE III as a possible reason for a bias. The SAGE III effective radius is based on a three-wavelength algorithm while the SAGE II product, which has fewer channels, is based on a two-wavelength algorithm. Additionally, the latter algorithm requires an a priori assumption of the geometric standard deviation. Therefore, we repeat the retrieval of the effective radius from SAGE III data using the two-wavelength retrieval algorithm (DWE) with different a priori geometric standard deviations (1.5 and 1.6) as
575 well as two different wavelength combinations (520/1021 nm and 449/1544 nm).

The change from a three- to a two-wavelength retrieval algorithm changes the effective radii depending on the mismatch between the assumed (DWE) and the retrieved (TWE) geometric standard deviation. The latter decreases on a yearly average from 1.66 in 2003 to 1.61 in 2004 and to 1.57 in 2005 (not shown). Assuming a geometric standard deviation of 1.5 and using the wavelength pair 520/1021 nm, the DWE approach yields effective radii that are 0.01 μm (2005) to 0.03 μm (2003) larger

580 than those from the TWE algorithm (Fig. 9). Better agreement between TWE and DWE data is achieved when a geometric standard deviation of 1.6 is assumed, especially in year 2004. The positive trend in effective radii as seen by the SAGE III TWE approach disappears when using the DWE approach. The selection of the wavelength pair has only minor influence on the retrieved effective radius (not shown). Remarkable is the difference of about 0.02 μm in the effective radius between SAGE II and SAGE III when using the identical retrieval algorithm.

585 To conclude, the a priori assumptions may slightly distort the retrieval data. However, the comparison of SAGE II and SAGE III data from the same retrieval algorithm indicates that the individual retrieval algorithms – and the a priori assumptions – are not the only reason for the systematic biases in the effective radius.

8.2.2 Varying measurement sensitivities

Another reason can be found in the different sensitivities of limb scatter and occultation measurements to stratospheric aerosol

590 particle sizes (e. g., Thomason and Poole, 1993; Rieger et al., 2014; Malinina et al., 2019; von Savigny and Hoffmann, 2020). While the transmitted solar radiance measured in the occultation geometry depends only on the aerosol extinction coefficient, the scattered radiation measured in limb geometry depends at a first approximation on the product of the aerosol phase function and the aerosol scattering coefficient, both of which are a function of the aerosol PSD. Thus, limb radiances in the visible and near-infrared range are more sensitive to the aerosol size than occultation measurements. Towards smaller particles, the sensi-

595 tivity decreases and falls below the detection limit faster for occultation measurements than for limb measurements (Malinina et al., 2019). As a result, small particles of a certain size can still be detected in limb geometry, but not in occultation geometry.

This fact might lead to larger particle sizes retrieved from occultation measurements than from limb scatter measurements, but only in cases where the aerosol loading is dominated by small particles and the assumed PSD shape in the retrieval algorithm differs from the true one (von Savigny and Hoffmann, 2020). This might explain at least a part of the difference in the effective

600 radius between SAGE II and SCIAMACHY, but contradicts with the similar values from SAGE III and SCIAMACHY.

The similar effective radius values of SAGE II and OPC in the Pinatubo post-eruption phase do not contradict but support the theory of varying measurement sensitivities being responsible for the bias. The Pinatubo eruption broadened the stratospheric aerosol particle size range (Bingen et al., 2004) and thus weakened the impact of very small particles on satellite observations. This reduced the effect of the different measurement sensitivities and thus the bias in effective radii between limb scatter and

605 occultation measurements.

Note that the comparison of retrieved extinction coefficients is not significantly influenced by the different sensitivities of limb scatter and occultation measurements. According to Eq. 4, the extinction coefficient is determined by the number density and optical cross section. Thus, larger particles contribute much stronger to the extinction coefficient than small ones. For the former, the difference in the sensitivity of limb scatter and occultation measurements to aerosols is small (Rieger et al., 2019).

8.2.3 Etalon effect

All solar occultation spectra measured with SAGE III-M3M are influenced by an etalon effect produced by a solar attenuator plate in the entrance optics. The solar attenuator was a neutral density filter where one side should be wedged by less than 1 arcmin. Due to the actual plane-parallel alignment of both filter sides, the attenuator acted like an etalon and caused interference patterns on the charge-coupled device (CCD) image sensor.

Thomason et al. (2010) have reported on an impact of the etalon effect on the water vapor retrieval. An additional influence of this effect on the extinction coefficient retrieval cannot be excluded. We compared the 520 to 1020-nm extinction ratios of SAGE II with respective 520 to 1021-nm extinction ratios of SAGE III. The latter were found to be greater due to lower Ext(1021 nm) values. It is not obvious, whether the SAGE II or the SAGE III extinction coefficients are closer to the truth, but a possibly underestimated SAGE III Ext(1021 nm) might be attributed to the etalon effect.

Since the interference pattern of the etalon affects the measured SAGE III signal over the entire wavelength spectrum, it would be conceivable that extinction coefficients of other wavelengths are also affected. The possibly altered extinction coefficients used for the SAGE III TWE approach (5.3) would lead to distorted effective radii. An accurate analysis and correction of the distortion is not feasible because the etalon effect depends on the etalon temperature and radiation wavelength, which prevents its quantification (Thomason et al., 2010).

8.3 Natural aerosol perturbations

Sulfur-rich volcanic eruptions and biomass burning events significantly enlarge the aerosol number density in the stratosphere. This increase is not considered at all during the retrieval process - the number density profile for aerosol background conditions (Sect. 4) is still assumed. Thus, the retrieval may return intensified deviating or incorrect PSD parameters. The retrieved median radii and geometric standard deviations should therefore be considered with caution in areas with high aerosol loading. However, due to the anti-correlation of the uncertainties of the median radius r_{g} and the geometric standard deviation σ_{g} - an underestimation of r_{g} is attended by an overestimation of σ_{g} and vice versa -, the uncertainties in the aerosol extinction coefficient and the effective radius might still remain small. A successful comparison of the SCIAMACHY-retrieved extinction coefficient and effective radius with model simulations after the Manam (2005) and Sarychev eruption (2009) confirms this statement (not shown).

It should be noted that in layers with strong aerosol perturbations, an adaptation of the a priori covariance would be worthwhile. The strength of regularization correlates especially with the aerosol particle size. Therefore, in some cases of large aerosol concentrations, a smaller a priori covariance may be required to keep the retrieval stable.

9 Conclusions

A global data set of stratospheric aerosol characteristics has been obtained from SCIAMACHY limb observations. It contains the median radius, the geometric standard deviation, the extinction coefficient, and the effective radius between 18 and 35 km

altitude. The median radius and the geometric standard deviation are directly retrieved by a multi-wavelength non-linear regularized inversion assuming a fixed number density profile. The extinction coefficient at 525, 750, and 1020 nm and the effective radius are subsequently calculated from these PSD parameters. All obtained aerosol characteristics depend only marginally on the surface albedo since the PSD retrieval employs the pre-retrieved surface albedo from SCIAMACHY nadir observations.

645   A sensitivity study based on synthetic retrievals clearly demonstrates the operational capability of the SCIAMACHY retrieval algorithm. However, the assumption of a Lambertian surface and a number density profile in the algorithm compromises an accurate retrieval. The Lambertian surface assumption introduces an uncertainty of about 11 % (4 %) in the retrieved median radius (geometric standard deviation), depending on the anisotropy of the surface. Errors in the pre-assumed number density profile control the quality of the retrieved PSD parameters. Furthermore, the results for the median radius and geometric

650 standard deviation are fully reliable only in the northern hemisphere. Here, limb radiances are sufficiently sensitive to aerosols so that both parameters can be retrieved separately. Nevertheless, the extinction coefficient and the effective radius obtained from a combination of the median radius and the geometric standard deviation are also valid in the southern hemisphere.

     The SCIAMACHY-retrieved and calculated aerosol characteristics have been evaluated with respective balloon-borne measurements over Wyoming as well as global satellite products from SAGE II, SAGE III-M3M, and OSIRIS. The median ra-

655 dius differs by less than 27 % and the geometric standard deviation by less than 11 % from balloon-borne measurements and SAGE III retrievals. In case of the balloon data comparison, a more accurate a priori number density profile can usually reduce the differences by more than a factor of 2. SCIAMACHY extinction coefficients at 750 nm deviate by less than 35 % from the other available satellite data products. This deviation is smaller than when comparing SAGE II, SAGE III-M3M, and OSIRIS data with the extinction coefficient from the SCIAMACHY retrieval version 1.4 (Rieger et al., 2018). The effective radii from

660 SCIAMACHY, balloon-borne measurements, and SAGE III agree within about 18 %.

     Particularly worth mentioning is the distinct bias between the effective radius from SAGE II and that from SCIAMACHY and SAGE III. At 21.7 km altitude, the bias is 0.04-0.05 µm and can not be explained by the different types of the retrieval algorithms applied. An incorrect choice of a priori assumptions, different sensitivity of limb and occultation observations for aerosols, and a potential distortion of SAGE III-M3M measurements due to the etalon effect are discussed as potential reasons.

665 However, a clear identification of the cause is hindered by the fact that the true effective radii are not known.

     The aerosol effective radius and extinction coefficients at 525, 750, and 1020 nm wavelengths are publicly available at "link". This data set significantly expands the limited knowledge of stratospheric aerosol properties and enables a better understanding of aerosol microphysical processes. Currently, the retrieval algorithm is being adapted with the goal to derive all three parameters of the lognormal PSD simultaneously, namely the median radius, the geometric standard deviation, and the number

670 density, from SCIAMACHY observations. Without any pre-assumption on the PSD parameters, the retrieval can provide lower uncertainties. It will result in more reliable PSD parameters that can be used independently of each other for interpretation purposes, at least in the northern hemisphere.

Appendix A: Relationship between normal and lognormal unimodal PSD

A unimodal normal size distribution:

$$n(r) = \frac{\mathrm{d}\,N}{\mathrm{d}\,r} = \frac{N}{\sqrt{2\pi}\,\sigma_0} \exp\left(-\frac{(r-\mu_0)^2}{2\,\sigma_0^2}\right) \tag{A1}$$

is defined by the total number density N, the arithmetic mean μ_0, and the standard deviation σ_0. However, stratospheric aerosols are better represented by a lognormal PSD. Substitution of r by $\ln r$ into Eq. (A1) yields:

$$n(r) = \frac{\mathrm{d}\,N(\ln r)}{\mathrm{d}\,r} = \frac{\mathrm{d}\,N(\ln r)}{\mathrm{d}\,(\ln r)}\frac{\mathrm{d}\,(\ln r)}{\mathrm{d}\,r} = \frac{\mathrm{d}\,N(\ln r)}{\mathrm{d}\,(\ln r)}\frac{1}{r} = \frac{N}{\sqrt{2\pi}\,\sigma^* r} \exp\left(-\frac{(\ln r - \mu^*)^2}{2\,\sigma^{*2}}\right), \tag{A2}$$

where μ^* and σ^* are the arithmetic mean and the arithmetic standard deviation of the PSD in logarithmic space (compare with Eq. (A1)):

$$\mu^* = \ln r_g \quad \sigma^* = \ln \sigma_{\mathrm{g}}. \tag{A3}$$

The variables r_g and σ_{g} are the geometric mean and the geometric standard deviation. Their names are evident as a geometric parameter is the equivalent of the arithmetic parameter in the logarithmic space:

$$r_{\mathrm{g}} = \exp\left(\ln\left(\sqrt[m]{r_1\,r_2\,r_3\ldots r_{\mathrm{m}}}\right)\right) = \exp\left(\frac{1}{m}\sum_{i=1}^{m}\ln r_{\mathrm{i}}\right) = \exp(\mu^*), \tag{A4}$$

$$\sigma_{\mathrm{g}} = \exp\left(\sqrt{\frac{1}{m}\sum_{i=1}^{m}(\ln r_{\mathrm{i}} - \ln r_{\mathrm{g}})^2}\right) = \exp(\sigma^*), \tag{A5}$$

where r_{i} are a set of m particle radii.

Since r_{g} and σ_{g} represent the maximum and dispersion of the PSD in the logarithmic space, it is more convenient to use the mode radius R_{mod} and the width w instead, which represent the maximum and spread of the PSD in the linear space:

$$R_{\mathrm{mod}} = \frac{r_{\mathrm{g}}}{\exp(\ln^2 \sigma_{\mathrm{g}})}, \tag{A6}$$

$$w^2 = [\exp(\ln^2 \sigma_{\mathrm{g}}) - 1]\exp(2\ln r_g + \ln^2 \sigma_{\mathrm{g}}). \tag{A7}$$

The square of the width, w^2, is also called arithmetic variance. Nevertheless, we will refer to r_{g} and σ_{g} in this paper, since both products are direct results of the SCIAMACHY retrieval algorithm (Sect. 4) and independent of each other.

Data availability. SCIAMACHY v2.0 extinction coefficients and effective radii are available at link?. SCIAMACHY v2.0 PSDs are available on request. SCIAMACHY v1.4 is available after registration at https://www.iup.uni-bremen.de/scia-arc/. Balloon-borne measurements are published in Deshler (2023), SAGE II v7.0 and SAGE III-M3M v4.0 at https://asdc.larc.nasa.gov/, and OSIRIS v7 at https://arg.usask.ca/docs/osiris_v7/. SAGE II and SAGE III aerosol characteristics based on the DWE and TWE approach will be made available on request.

Author contributions. CP optimized the SCIAMACHY retrieval algorithm, performed test calculations, retrieved SCIAMACHY v2.0 aerosol products, performed the data analysis and comparison, and wrote the manuscript. FW retrieved and provided aerosol products from SAGE II DWE and SAGE III TWE/DWE, provided valuable contribution to the SCIAMACHY - SAGE II/III comparison, and wrote Sect. 5.2 and 5.3 of the manuscript. AR developed the retrieval software and retrieved and provided the effective Lambertian surface albedo from SCIA-MACHY nadir radiances. TD helped with access to the publicly available OPC measurements and calculated OPC-measured unimodal lognormal PSDs. EM, LR, and AEB provided extinction coefficients from SCIAMACHY v1.4 and OSIRIS and gave scientific advice in limb scattering retrievals. AR, CvS, and JPB initiated and supervised the project. All authors contributed to the discussions, provided critical feedback on the manuscript, and added valuable suggestions to the final manuscript.

Competing interests. CvS is a member of the editorial board of AMT. The peer-review process was guided by an independent editor, and the authors have also no other competing interests to declare.

Acknowledgements. This research has been funded in parts by the Deutsche Forschungsgemeinschaft (DFG) via the Research Unit VolImpact (grant no. 398006378), by the ESA via CREST project, and by the University and State of Bremen. The balloon-borne measurements were completed under funding the US National Science Foundation and National Aeronautics and Space Administration. All SCIAMACHY v2.0 aerosol retrievals reported here were performed on HPC facilities of the IUP, University of Bremen, funded under DFG/FUGG grant INST 144/379-1 and INST 144/493-1. We thank Larry W. Thomason for his SAGE II and SAGE III expertise.

References

Andersson, S. M., Martinsson, B. G., Vernier, J.-P., Friberg, J., Brenninkmeijer, C. A. M., Hermann, M., Van Velthoven, P. F. J., and Zahn, A.: Significant radiative impact of volcanic aerosol in the lowermost stratosphere, Nature communications, 6, 1–8, 2015.

715 Ångström, A.: On the atmospheric transmission of sun radiation and on dust in the air, Geografiska Annaler, 11, 156–166, 1929.

Arfeuille, F., Luo, B. P., Heckendorn, P., Weisenstein, D., Sheng, J.-X., Rozanov, E., Schraner, M., Brönnimann, S., Thomason, L. W., and Peter, T.: Modeling the stratospheric warming following the Mt. Pinatubo eruption: uncertainties in aerosol extinctions, Atmospheric Chemistry and Physics, 13, 11 221–11 234, 2013.

Aubry, T. J., Toohey, M., Marshall, L., Schmidt, A., and Jellinek, A. M.: A new volcanic stratospheric sulfate aerosol forcing em-
720 ulator (EVA_H): Comparison with interactive stratospheric aerosol models, Journal of Geophysical Research: Atmospheres, 125, e2019JD031 303, 2020.

Bingen, C., Fussen, D., and Vanhellemont, F.: A global climatology of stratospheric aerosol size distribution parameters derived from SAGE II data over the period 1984–2000: 1. Methodology and climatological observations, Journal of Geophysical Research: Atmospheres, 109, 2004.

725 Bourassa, A. E., Degenstein, D. A., and Llewellyn, E. J.: Retrieval of stratospheric aerosol size information from OSIRIS limb scattered sunlight spectra, Atmospheric Chemistry and Physics, 8, 6375–6380, 2008.

Bourassa, A. E., Rieger, L. A., Zawada, D. J., Khaykin, S., Thomason, L. W., and Degenstein, D. A.: Satellite limb observations of unprece-dented forest fire aerosol in the stratosphere, Journal of Geophysical Research: Atmospheres, 124, 9510–9519, 2019.

Bovensmann, H., Burrows, J. P., Buchwitz, M., Frerick, J., Noël, S., Rozanov, V. V., Chance, K. V., and Goede, A. P. H.: SCIAMACHY:
730 Mission objectives and measurement modes, Journal of the atmospheric sciences, 56, 127–150, 1999.

Brühl, C., Lelieveld, J., Crutzen, P. J., and Tost, H.: The role of carbonyl sulphide as a source of stratospheric sulphate aerosol and its impact on climate, Atmospheric Chemistry and Physics, 12, 1239–1253, 2012.

Brühl, C., Lelieveld, J., Tost, H., Höpfner, M., and Glatthor, N.: Stratospheric sulfur and its implications for radiative forcing simulated by the chemistry climate model EMAC, Journal of Geophysical Research: Atmospheres, 120, 2103–2118, 2015.

735 Burrows, J. P., Hölzle, E., Goede, A. P. H., Visser, H., and Fricke, W.: SCIAMACHY—Scanning imaging absorption spectrometer for atmospheric chartography, Acta Astronautica, 35, 445–451, 1995.

Chylek, P., Folland, C., Klett, J. D., and Dubey, M. K.: CMIP5 climate models overestimate cooling by volcanic aerosols, Geophysical Research Letters, 47, e2020GL087 047, 2020.

Colose, C. M., LeGrande, A. N., and Vuille, M.: Hemispherically asymmetric volcanic forcing of tropical hydroclimate during the last
740 millennium, Earth System Dynamics, 7, 681–696, 2016.

DallaSanta, K., Orbe, C., Rind, D., Nazarenko, L., and Jonas, J.: Response of the Quasi-Biennial Oscillation to Historical Volcanic Eruptions, Geophysical Research Letters, 48, e2021GL095 412, 2021.

Damadeo, R. P., Zawodny, J. M., Thomason, L. W., and Iyer, N.: SAGE version 7.0 algorithm: application to SAGE II, Atmospheric Mea-surement Techniques, 6, 3539–3561, 2013.

745 Das, S., Colarco, P. R., Oman, L. D., Taha, G., and Torres, O.: The long-term transport and radiative impacts of the 2017 British Columbia pyrocumulonimbus smoke aerosols in the stratosphere, Atmospheric Chemistry and Physics, 21, 12 069–12 090, 2021.

Deshler, T.: A review of global stratospheric aerosol: Measurements, importance, life cycle, and local stratospheric aerosol, Atmospheric Research, 90, 223–232, 2008.

Deshler, T.: University of Wyoming Stratospheric Aerosol Measurements. University of Wyoming. Collection., https://doi.org/https://doi.org/10.15786/c.6379371.v1, 2023.

Deshler, T., Hervig, M. E., Hofmann, D. J., Rosen, J. M., and Liley, J. B.: Thirty years of in situ stratospheric aerosol size distribution measurements from Laramie, Wyoming (41° N), using balloon-borne instruments, Journal of Geophysical Research: Atmospheres, 108, 2003.

Deshler, T., Anderson-Sprecher, R., Jäger, H., Barnes, J., Hofmann, D. J., Clemesha, B., Simonich, D., Osborn, M., Grainger, R. G., and Godin-Beekmann, S.: Trends in the nonvolcanic component of stratospheric aerosol over the period 1971–2004, Journal of Geophysical Research: Atmospheres, 111, 2006.

Deshler, T., Luo, B., Kovilakam, M., Peter, T., and Kalnajs, L. E.: Retrieval of aerosol size distributions from in situ particle counter measurements: Instrument counting efficiency and comparisons with satellite measurements, Journal of Geophysical Research: Atmospheres, 124, 5058–5087, 2019.

Ebert, M., Weigel, R., Kandler, K., Günther, G., Molleker, S., Grooß, J.-U., Vogel, B., Weinbruch, S., and Borrmann, S.: Chemical analysis of refractory stratospheric aerosol particles collected within the arctic vortex and inside polar stratospheric clouds, Atmospheric Chemistry and Physics, 16, 8405–8421, 2016.

Fahey, D. W., Kawa, S. R., Woodbridge, E. L., Tin, P., Wilson, J. C., Jonsson, H. H., Dye, J. E., Baumgardner, D., Borrmann, S., Toohey, D. W., Avallone, L. M., Proffitt, M. H., Margitan, J., Loewenstein, M., Podolske, J. R., Salawitch, R. J., Wofsy, S. C., Ko, M. K. W., Anderson, D. E., Schoeber, M. R., and Chan, K. R.: In situ measurements constraining the role of sulphate aerosols in mid-latitude ozone depletion, Nature, 363, 509–514, 1993.

Friberg, J., Martinsson, B. G., Andersson, S. M., and Sandvik, O. S.: Volcanic impact on the climate–the stratospheric aerosol load in the period 2006–2015, Atmospheric Chemistry and Physics, 18, 11 149–11 169, 2018.

Fussen, D. and Bingen, C.: A volcanism dependent model for the extinction profile of stratospheric aerosols in the UV-visible range, Geophysical research letters, 26, 703–706, 1999.

Gottwald, M. and Bovensmann, H.: SCIAMACHY-Exploring the changing Earth's Atmosphere, Springer Science & Business Media, 2010.

Grieser, J. and Schönwiese, C.-D.: Parameterization of spatio-temporal patterns of volcanic aerosol induced stratospheric optical depth and its climate radiative forcing, Atmósfera, 12, 1999.

Hermanson, L., Bilbao, R., Dunstone, N., Ménégoz, M., Ortega, P., Pohlmann, H., Robson, J. I., Smith, D. M., Strand, G., Timmreck, C., Yeager, S., and Danabasoglu, G.: Robust multiyear climate impacts of volcanic eruptions in decadal prediction systems, Journal of Geophysical Research: Atmospheres, 125, e2019JD031 739, 2020.

Hess, M., Koepke, P., and Schult, I.: Optical properties of aerosols and clouds: The software package OPAC, Bulletin of the American meteorological society, 79, 831–844, 1998.

Iles, C. E., Hegerl, G. C., Schurer, A. P., and Zhang, X.: The effect of volcanic eruptions on global precipitation, Journal of Geophysical Research: Atmospheres, 118, 8770–8786, 2013.

Khodri, M., Izumo, T., Vialard, J., Janicot, S., Cassou, C., Lengaigne, M., Mignot, J., Gastineau, G., Guilyardi, E., Lebas, N., Robock, A., and McPhaden, M. J.: Tropical explosive volcanic eruptions can trigger El Niño by cooling tropical Africa, Nature communications, 8, 778, 2017.

Kloss, C., Berthet, G., Sellitto, P., Ploeger, F., Taha, G., Tidiga, M., Eremenko, M., Bossolasco, A., Jégou, F., Renard, J.-B., et al.: Stratospheric aerosol layer perturbation caused by the 2019 Raikoke and Ulawun eruptions and their radiative forcing, Atmospheric Chemistry and Physics, 21, 535–560, 2021.

Kovilakam, M. and Deshler, T.: On the accuracy of stratospheric aerosol extinction derived from in situ size distribution measurements and surface area density derived from remote SAGE II and HALOE extinction measurements, Journal of Geophysical Research: Atmospheres, 120, 8426–8447, 2015.

790 Kovilakam, M., Thomason, L. W., Ernest, N., Rieger, L., Bourassa, A., and Millán, L.: The global space-based stratospheric aerosol climatology (version 2.0): 1979–2018, Earth System Science Data, 12, 2607–2634, 2020.

Kremser, S., Thomason, L. W., von Hobe, M., Hermann, M., Deshler, T., Timmreck, C., Toohey, M., Stenke, A., Schwarz, J. P., Weigel, R., Fueglistaler, S., Prata, F. J., Vernier, J.-P., Schlager, H., Barnes, J. E., Antuna-Marrero, J.-C., Fairlie, D., Palm, M., Mahieu, E., Notholt, J., Rex, M., Bingen, C., Vanhellemont, F., Bourassa, A., Plane, J. M. C., Klocke, D., Carn, S. A., Clarisse, L., Trickl, T., Neely, R., James,
795 A. D., Rieger, L., Wilson, J. C., and Meland, B.: Stratospheric aerosol—Observations, processes, and impact on climate, Reviews of Geophysics, 54, 278–335, 2016.

Liu, F., Chai, J., Wang, B., Liu, J., Zhang, X., and Wang, Z.: Global monsoon precipitation responses to large volcanic eruptions, Scientific reports, 6, 24 331, 2016.

Llewellyn, E. J., Lloyd, N. D., Degenstein, D. A., Gattinger, R. L., Petelina, S. V., Bourassa, A. E., Wiensz, J. T., Ivanov, E. V., McDade,
800 I. C., Solheim, B. H., McConnell, J. C., Haley, C. S., von Savigny, C., Sioris, C. E., McLinden, C. A., Griffioen, E., Kaminski, J., Evans, W. F. J., Puckrin, E., Strong, K., Wehrle, V., Hum, R. H., Kendall, D. J. W., Matsushita, J., Murtagh, D. P., Brohede, S., Stegman, J., Witt, G., Barnes, G., Payne, W. F., Piché, L., Smith, K., Warshaw, G., Deslauniers, D. L., Marchand, P., Richardson, E. H., King, R. A., Wevers, I., McCreath, W., Kyrölä, E., Oikarinen, L., Leppelmeier, G. W., Auvinen, H., Mégie, G., Hauchecorne, A., Lefèvre, F., de La Nöe, J., Ricaud, P., Frisk, U., Sjoberg, F., von Schéele, F., and Nordh, L.: The OSIRIS instrument on the Odin spacecraft, Canadian Journal of
805 Physics, 82, 411–422, 2004.

Lorente, A., Boersma, K. F., Stammes, P., Tilstra, L. G., Richter, A., Yu, H., Kharbouche, S., and Muller, J.-P.: The importance of surface reflectance anisotropy for cloud and NO_2 retrievals from GOME-2 and OMI, Atmospheric Measurement Techniques, 11, 4509–4529, 2018.

Lucht, W., Schaaf, C. B., and Strahler, A. H.: An algorithm for the retrieval of albedo from space using semiempirical BRDF models, IEEE
810 Transactions on Geoscience and Remote sensing, 38, 977–998, 2000.

Malinina, E., Rozanov, A., Rozanov, V., Liebing, P., Bovensmann, H., and Burrows, J. P.: Aerosol particle size distribution in the stratosphere retrieved from SCIAMACHY limb measurements, Atmospheric Measurement Techniques, 11, 2085–2100, 2018.

Malinina, E., Rozanov, A., Rieger, L., Bourassa, A., Bovensmann, H., Burrows, J. P., and Degenstein, D.: Stratospheric aerosol characteristics from space-borne observations: extinction coefficient and Ångström exponent, Atmospheric Measurement Techniques, 12, 3485–3502,
815 2019.

Malinina, E., Rozanov, A., Niemeier, U., Wallis, S., Arosio, C., Wrana, F., Timmreck, C., von Savigny, C., and Burrows, J. P.: Changes in stratospheric aerosol extinction coefficient after the 2018 Ambae eruption as seen by OMPS-LP and MAECHAM5-HAM, Atmospheric Chemistry and Physics, 21, 14 871–14 891, https://doi.org/10.5194/acp-21-14871-2021, 2021.

Marshall, L. R., Maters, E. C., Schmidt, A., Timmreck, C., Robock, A., and Toohey, M.: Volcanic effects on climate: recent advances and
820 future avenues, Bulletin of Volcanology, 84, 1–14, 2022.

Mauldin III, L. E., Zaun, N. H., McCormick Jr, M. P., Guy, J. H., and Vaughn, W. R.: Stratospheric Aerosol and Gas Experiment II instrument: A functional description, Optical Engineering, 24, 307–312, 1985.

McCormick, M. P.: SAGE II: an overview, Advances in space research, 7, 219–226, 1987.

McCormick, M. P. and Chu, W. P.: Stratospheric aerosol and gas experiment III (SAGE III): data product user's guide. Version 1.5, 2004.

825 McCormick, M. P., Thomason, L. W., and Trepte, C. R.: Atmospheric effects of the Mt Pinatubo eruption, Nature, 373, 399–404, 1995.

McLinden, C. A., McConnell, J. C., McElroy, C. T., and Griffioen, E.: Observations of stratospheric aerosol using CPFM polarized limb radiances, Journal of the atmospheric sciences, 56, 233–240, 1999.

McLinden, C. A., Bourassa, A. E., Brohede, S., Cooper, M., Degenstein, D. A., Evans, W. J. F., Gattinger, R. L., Haley, C. S., Llewellyn, E. J., Lloyd, N. D., Loewen, P., Martin, R. V., McConnell, J. C., McDade, I. C., Murtagh, D., Rieger, L., von Savigny, C., Sheese, P. E.,
830 Sioris, C. E., Solheim, B., and Strong, K.: OSIRIS: A decade of scattered light, Bulletin of the American Meteorological Society, 93, 1845–1863, 2012.

Mei, L., Rozanov, V., Rozanov, A., and Burrows, J. P.: SCIATRAN software package (V4.6): update and further development of aerosol, clouds, surface reflectance databases and models, Geoscientific Model Development, 16, 1511–1536, https://doi.org/10.5194/gmd-16-1511-2023, 2023.

835 Mills, M. J., Schmidt, A., Easter, R., Solomon, S., Kinnison, D. E., Ghan, S. J., Neely III, R. R., Marsh, D. R., Conley, A., Bardeen, C. G., and Gettelman, A.: Global volcanic aerosol properties derived from emissions, 1990–2014, using CESM1 (WACCM), Journal of Geophysical Research: Atmospheres, 121, 2332–2348, 2016.

Mishchenko, M. I. and Travis, L. D.: Satellite retrieval of aerosol properties over the ocean using polarization as well as intensity of reflected sunlight, Journal of Geophysical Research: Atmospheres, 102, 16 989–17 013, 1997.

840 Ohneiser, K., Ansmann, A., Baars, H., Seifert, P., Barja, B., Jimenez, C., Radenz, M., Teisseire, A., Floutsi, A., Haarig, M., Foth, A., Chudnovsky, A., Engelmann, R., Zamorano, F., Bühl, J., and Wandinger, U. o.: Smoke of extreme Australian bushfires observed in the stratosphere over Punta Arenas, Chile, in January 2020: optical thickness, lidar ratios, and depolarization ratios at 355 and 532 nm, Atmospheric Chemistry and Physics, 20, 8003–8015, 2020.

Oxford University: Department of Physics: Earth Observation Data Group: Mie Scattering Routines, http://eodg.atm.ox.ac.uk/MIE/index.
845 html, accessed September 26, 2022, 2022.

Palmer, K. F. and Williams, D.: Optical constants of sulfuric acid; application to the clouds of Venus?, Applied Optics, 14, 208–219, 1975.

Pausata, F. S. R., Chafik, L., Caballero, R., and Battisti, D. S.: Impacts of high-latitude volcanic eruptions on ENSO and AMOC, Proceedings of the National Academy of Sciences, 112, 13 784–13 788, 2015.

Reeves, J. M., Wilson, J. C., Brock, C. A., and Bui, T. P.: Comparison of aerosol extinction coefficients, surface area density, and volume
850 density from SAGE II and in situ aircraft measurements, Journal of Geophysical Research: Atmospheres, 113, 2008.

Rieger, L. A., Bourassa, A. E., and Degenstein, D. A.: Stratospheric aerosol particle size information in Odin-OSIRIS limb scatter spectra, Atmospheric Measurement Techniques, 7, 507–522, 2014.

Rieger, L. A., Malinina, E. P., Rozanov, A. V., Burrows, J. P., Bourassa, A. E., and Degenstein, D. A.: A study of the approaches used to retrieve aerosol extinction, as applied to limb observations made by OSIRIS and SCIAMACHY, Atmospheric Measurement Techniques,
855 11, 3433–3445, 2018.

Rieger, L. A., Zawada, D. J., Bourassa, A. E., and Degenstein, D. A.: A multiwavelength retrieval approach for improved OSIRIS aerosol extinction retrievals, Journal of Geophysical Research: Atmospheres, 124, 7286–7307, 2019.

Roberts, R. R., Milov, Y. G., Zonov, Y. V., Salikhov, R. S., and Charles, L. B.: IAN-USA SAGE III/Meteor-3M project, Acta astronautica, 38, 479–485, 1996.

860 Robock, A., MacMartin, D. G., Duren, R., and Christensen, M. W.: Studying geoengineering with natural and anthropogenic analogs, Climatic Change, 121, 445–458, 2013.

Rodgers, C. D.: Inverse methods for atmospheric sounding: theory and practice, vol. 2, World scientific, 2000.

Rozanov, V. V., Rozanov, A. V., Kokhanovsky, A. A., and Burrows, J. P.: Radiative transfer through terrestrial atmosphere and ocean: Software package SCIATRAN, Journal of Quantitative Spectroscopy and Radiative Transfer, 133, 13–71, 2014.

865 Sato, M., Hansen, J. E., Lacis, A., McCormick, M. P., Pollack, J. B., Thomason, L., and Bourassa, A.: Forcings in GISS Climate Model - Stratospheric Aerosol Optical Thickness, https://data.giss.nasa.gov/modelforce/strataer/, accessed September 21, 2022, 2016.

Schaepman-Strub, G., Schaepman, M. E., Painter, T. H., Dangel, S., and Martonchik, J. V.: Reflectance quantities in optical remote sensing—Definitions and case studies, Remote sensing of environment, 103, 27–42, 2006.

Schallock, J., Brühl, C., Bingen, C., Höpfner, M., Rieger, L., and Lelieveld, J.: Reconstructing volcanic radiative forcing since 1990, using a
870 comprehensive emission inventory and spatially resolved sulfur injections from satellite data in a chemistry-climate model, Atmospheric Chemistry and Physics, 23, 1169–1207, 2023.

Sellitto, P., Belhadji, R., Kloss, C., and Legras, B.: Radiative impacts of the Australian bushfires 2019–2020–Part 1: Large-scale radiative forcing, Atmospheric Chemistry and Physics, 22, 9299–9311, 2022.

Siddaway, J. M. and Petelina, S. V.: Transport and evolution of the 2009 Australian Black Saturday bushfire smoke in the lower stratosphere
875 observed by OSIRIS on Odin, Journal of Geophysical Research: Atmospheres, 116, 2011.

Solomon, S., Portmann, R. W., Garcia, R. R., Thomason, L. W., Poole, L. R., and McCormick, M. P.: The role of aerosol variations in anthropogenic ozone depletion at northern midlatitudes, Journal of Geophysical Research: Atmospheres, 101, 6713–6727, 1996.

Steele, H. M. and Hamill, P.: Effects of temperature and humidity on the growth and optical properties of sulphuric acid—water droplets in the stratosphere, Journal of aerosol science, 12, 517–528, 1981.

880 Stenchikov, G. L., Kirchner, I., Robock, A., Graf, H.-F., Antuna, J. C., Grainger, R. G., Lambert, A., and Thomason, L.: Radiative forcing from the 1991 Mount Pinatubo volcanic eruption, Journal of Geophysical Research: Atmospheres, 103, 13 837–13 857, 1998.

Tejedor, E., Steiger, N., Smerdon, J. E., Serrano-Notivoli, R., and Vuille, M.: Global temperature responses to large tropical volcanic eruptions in paleo data assimilation products and climate model simulations over the last millennium, Paleoceanography and Paleoclimatology, 36, e2020PA004 128, 2021.

885 Thomason, L. and Peter, T.: SPARC Assessment of Stratospheric Aerosol Properties (ASAP), Tech. rep., SPARC, http://www.sparc-climate. org/publications/sparc-reports/, accessed September 26, 2022, 2006.

Thomason, L. W. and Poole, L. R.: Use of stratospheric aerosol properties as diagnostics of Antarctic vortex processes, Journal of Geophysical Research: Atmospheres, 98, 23 003–23 012, 1993.

Thomason, L. W., Burton, S. P., Luo, B.-P., and Peter, T.: SAGE II measurements of stratospheric aerosol properties at non-volcanic levels,
890 Atmospheric Chemistry and Physics, 8, 983–995, 2008.

Thomason, L. W., Moore, J. R., Pitts, M. C., Zawodny, J. M., and Chiou, E. W.: An evaluation of the SAGE III version 4 aerosol extinction coefficient and water vapor data products, Atmospheric Chemistry and Physics, 10, 2159–2173, 2010.

Thomason, L. W., Ernest, N., Millán, L., Rieger, L., Bourassa, A., Vernier, J.-P., Manney, G., Luo, B., Arfeuille, F., and Peter, T.: A global space-based stratospheric aerosol climatology: 1979–2016, Earth System Science Data, 10, 469–492, 2018.

895 Toohey, M., Krüger, K., Bittner, M., Timmreck, C., and Schmidt, H.: The impact of volcanic aerosol on the Northern Hemisphere stratospheric polar vortex: mechanisms and sensitivity to forcing structure, Atmospheric Chemistry and Physics, 14, 13 063–13 079, 2014.

Toohey, M., Stevens, B., Schmidt, H., and Timmreck, C.: Easy Volcanic Aerosol (EVA v1. 0): an idealized forcing generator for climate simulations, Geoscientific Model Development, 9, 4049–4070, 2016.

Ugolnikov, O. S. and Maslov, I. A.: Investigations of the background stratospheric aerosol using multicolor wide-angle measurements of the
900 twilight glow background, Cosmic Research, 56, 85–93, 2018.

Vignati, E., Wilson, J., and Stier, P.: M7: An efficient size-resolved aerosol microphysics module for large-scale aerosol transport models, Journal of Geophysical Research: Atmospheres, 109, 2004.

von Savigny, C. and Hoffmann, C. G.: Issues related to the retrieval of stratospheric-aerosol particle size information based on optical measurements, Atmospheric Measurement Techniques, 13, 1909–1920, 2020.

905 von Savigny, C., Ernst, F., Rozanov, A., Hommel, R., Eichmann, K.-U., Rozanov, V., Burrows, J. P., and Thomason, L. W.: Improved stratospheric aerosol extinction profiles from SCIAMACHY: validation and sample results, Atmospheric Measurement Techniques, 8, 5223–5235, 2015.

Warshaw, G., Desaulniers, D.-L., and Degenstein, D.: Optical design and performance of the Odin UV/visible spectrograph and infrared imager instrument, in: Proceedings of the 10th annual AIAA/Utah state university conference onsmall satellites, September 16–19, 1996.

910 Wrana, F., Von Savigny, C., Zalach, J., and Thomason, L. W.: Retrieval of stratospheric aerosol size distribution parameters using satellite solar occultation measurements at three wavelengths, Atmospheric Measurement Techniques, 14, 2345–2357, 2021.

Wurl, D., Grainger, R. G., McDonald, A. J., and Deshler, T.: Optimal estimation retrieval of aerosol microphysical properties from SAGE II satellite observations in the volcanically unperturbed lower stratosphere, Atmospheric Chemistry and Physics, 10, 4295–4317, 2010.

Yue, G. K. and Deepak, A.: Retrieval of stratospheric aerosol size distribution from atmospheric extinction of solar radiation at two wave-
915 lengths, Applied Optics, 22, 1639–1645, 1983.

Zalach, J., von Savigny, C., Langenbach, A., Baumgarten, G., Lübken, F.-J., and Bourassa, A.: Challenges in retrieving stratospheric aerosol extinction and particle size from ground-based RMR-LIDAR observations, Atmospheric Measurement Techniques Discussions, pp. 1–21, 2019.